Feasibility Study of Ferromagnetic Particulate Path Diversion in Additive Manufacturing

by

David Michael Bruce Dombroski

A thesis
presented to the University of Waterloo
in fulfillment of the
thesis requirement for the degree of
Master of Applied Science
in
Mechanical and Mechatronics Engineering

Waterloo, Ontario, Canada, 2018

Author's Declaration

I hereby declare that I am the sole author of this thesis. This is a true copy of the thesis, including any required final revisions, as accepted by my examiners.

I understand that my thesis may be made electronically available to the public.

Abstract

The use of electromagnetic actuator components typically involves a coil comprised of a stack-packed continuous winding, usually layered, and a core material of soft iron or at least a solenoid, similarly constructed, simply with an air core. These are used widely across, but not limited to, several industries such as automotive, aerospace, medical, and various electronics. Their application to additive manufacturing (AM), and in particular to improvement of catchment efficiency, is a somewhat newly ventured avenue and the use of permanent magnets in their place to simulate their presence is of similar vein.

The objective of this thesis is to introduce a novel but constructive approach to implement catchment efficiency improvement with regard to ferromagnetic particles by increasing their density in proximity to the melt pool through introduction of a magnetic (or electromagnetic) field. This field acts to produce a lensing or concentric constriction of the particle stream above, and as its contents near and enter the AM build zone. The particle dynamics and stream studied have a purely vertical initial velocity and steady flow rate. Not discussed are melt pool effects from the introduced magnetic field, or angled AM particle streams.

Four analytical methods to determine the magnetic (**B**) field either on or off the axis of a solenoid are first studied, then narrowed to two to verify Matlab programming from an established benchmark. A finite element (FEA) model is constructed to provide simulations and a soft iron particle is introduced to further determine validity of Matlab programming for both air core and iron core constructs. A similar process uses permanent magnets in place of a coil. A parametric sweep in the FEA software generates force data for post-processing in Matlab to produce particle displacement plots using differential equations to complete this technique.

The aforementioned simulation process serves as confirmation of particle path diversion and additional experimental validation is proposed. The experiments would substantiate particulate path diversions in the presence of the permanent magnet configuration, substituted for a coil configuration, to confirm the simulated construct to be authentic regarding its required particulate force effects.

Acknowledgements

First and foremost I would like to thank my faculty advisers/supervisors for their continued dedication in their approach to guide my efforts. Dr. Behrad Khamesee and Dr. Amir Khajepour regularly contributed to assist in interpreting the knowledge required to complete my efforts, keeping track of scope, and redirecting my efforts as this undertaking proceeded. I would also like to further thank Dr. Behrad Khamesee and Dr. Amir Khajepour as thesis readers, whose contribution was greatly appreciated throughout the many revisions, and my additional pre-seminar thesis readers Dr. Ehsan Toyserkani and Dr. Zhongchao Tan. Additionally, my thanks goes out to the staff and faculty of the University of Waterloo, especially those of the Mechanical and Mechatronics department. I am very pleased to have an institution of outstanding caliber in close locale to allow me to undertake at this elevated level. Further extended thanks goes to the University of Toronto Institute for Aerospace Studies (UTIAS) for providing the opportunity to commence my graduate studies, with my initial semester.

I would further like to express my thanks to the Canadian banking system for having the avenues to financial assistance that provided comfort and assurance that a personal undertaking of this magnitude could be achieved without undue stress given its duration. They are perhaps the most understanding collective I have ever had the pleasure of dealing with.

Many thanks go to my colleagues and close fellow researchers who aided in gaining immediate understanding of related subject material and computational efforts. Special mention goes out to Yuze Huang (Sam) for his dedicated assistance in experimental efforts in the laboratory environment. Much appreciation is directed to Haniyeh Fayazfar (Ramona) and the Multi-Scale Additive Manufacturing group (MSAM), headed by Dr. Ehsan Toyserkani, who granted permission to attend their bi-monthly seminars and provided a ready audience for presentation of subject material generated during my research efforts.

Additionally I would like to thank my family and community. Often overlooked they nonetheless provided much needed support and the knowledge that this would be given regardless, strengthened my resolve. Thank you all and I take comfort knowing my goals can be successfully achieved with your contributions and continued support towards a most positive result.

Dedication

This dedication goes out to all who have provided assistance to get me to where I am academically over the last decade or so. Special mention goes to the staff, fellow students, and faculty of Conestoga College, Institute of Technology and Advanced Learning where my most recent degree was assured, and those who acted as referees to allow me to continue with my efforts. Closest to my well-being is my immediate family. Thanks to you all for your continued understanding in my need to personally excel.

Table of Contents

List of Figures

List of Tables

List of Abbreviations

AC/DC alternating current/direct current 36

ACS air core solenoid 24, 25, 26, 27

AM additive manufacturing iii, 1, 2, 3, 5, 6, 7, 9, 11, 12, 15, 16, 23, 48, 49, 57, and 58

CAD computer aided design 2

CNC computer numerical control 17, 59, 61, 79

DLD direct laser deposition 2

FEA finite element analysis iii, 4, 18, 19, 21, 24, 35, 36, 37, 40, 41, 42, 45, 46, 47, 57

MIMO multiple input multiple output 12

MRI magnetic resonance imaging 12

MS Microsoft 20

PM permanent magnet 45, 46, 47, 49, 50, 51, 52, 53, 54, 55, 81

SISO single input single output 12

SLM selective laser melting 2, 17

List of Nomenclature

Chapter 2

P_e, y Catchment efficiency 7

A_c, A Area of the clad (vertical cross section of the powder melt), 7

S, v Scanning (traverse) speed, 7

ϱ Powder material density, 7

F, m' Powder feed (mass flow) rate, 7

η, η_p Catchment efficiency 8

$S_{jet}^{liq}, A_{jet}^{melt}$ Molten pool area, 8

S_{jet}, A_{jet} Substrate area impinged by the powder jet, 8

B Magnetic field, 13, 14. Also iii, 24-31, 34-37, 39, 44, 57, 78

H Magnetic field intensity, 14

M Magnetization, 14. Also 36, 78

Chapter 3

F_{drag}, F_D Aerodynamic drag force, 22, 23

$F_{magnetic}$, F_{mag} Magnetic force, 22, 23

ρ Particle density, 23

v Particle velocity relative to fluid, 23

C_D Aerodynamic drag coefficient, 23

A Frontal (cross sectional) area, 23

Chapter 4

On Axis

μ_0 Permeability of free space, 25, and throughout

I Current, 25, and throughout

a Coil radius, 25, 26, 27

z Height from coil center along z axis, 25, 26, 27

$\bar{B}$ Magnetic field strength, 25, 26, 27

N Number of coil turns, 26, 27

l Coil length, 26, 27

z' Integration variable, 26

Off Axis

In addition to above:

R Coil radius, 28

θ Angle $\vec{r}_P$ vector makes with z-axis, 28

φ' Angle $\vec{r}'$ vector makes with x-axis, 28

r Magnitude of $\vec{r}$, 28

y y-coordinate of point *P*, 28

z z-coordinate of point *P*, 28

P Point of interest, 28

Elliptic Integrals

B_0 Magnetic field strength at coil center, 30

B_x Magnetic field strength x-component at point of interest, 29, 30

B_r Magnetic field strength radial component at point of interest, 29, 30

Q Internal equation factor based on alpha and beta, 30

$E(k^2)$ Complete elliptic integral function of the second kind, 30

$K(k^2)$ Complete elliptic integral function of the first kind, 30

α Ratio of r over a, 30

β Ratio of x over a, 30

γ Ratio of x over r, 30

r Distance in the radial direction from the axis of the current loop to the field measurement point, 29, 30

a Loop radius, 29, 30

x Distance in the axial direction from the center of the current loop to the field measurement point;29, 30

Summations

$\boldsymbol{\mu}$ Permeability of free space, 31

$\boldsymbol{I}$ Resident electrical current, 31

$\boldsymbol{r_{Mth\_layer}}$ Radius of the Mth layer, 31

$\boldsymbol{z_{Nth\_turn}}$ Height of the Nth turn, 31

$\boldsymbol{P_z}$ Vertical coordinate of the point of interest, 31

$\boldsymbol{P_r}$ Radial coordinate of the point of interest, 31

$\Delta\boldsymbol{\theta}$ Theta increment/division chosen to develop accuracy, 31

$\boldsymbol{\varphi}$ Angle from the x-z plane to the plane containing P_z and P_r, 31

Force

$\boldsymbol{F}$ Electromagnetic force, 37

$\boldsymbol{M_x, M_y, M_z}$ Components of magnetization, 37

$\boldsymbol{B_{ext_x}, B_{ext_y}, B_{ext_z}}$ Components of magnetic field, 37

Magnetic Fields and Magnetic Field Gradients

The magnetic field equations used are as described in (4.18) to (4.22) on pages 38 to 39, similar to the Elliptic Integrals content provided, above. The magnetic field gradient content of Appendix E makes use of this information in addition to the following list, below.

$\boldsymbol{\frac{\partial}{\partial x}, \frac{\partial}{\partial y}, \frac{\partial}{\partial z}}$ Cartesian partial derivatives with respect to x, y, z, Appendix E

$\boldsymbol{B_x}$, $\boldsymbol{B_y}$, and $\boldsymbol{B_z}$ Cartesian components of magnetic field at point of interest, 39

Chapter 1
Introduction

Descriptively different from subtractive manufacturing where a usable part is literally carved out of a solid block of material, or blank, additive manufacturing is known to work by building an object up with the use of stratified, layer-by-layer construction. The precision of the form outline of such a part can be dictated by the resolution of such layers and this preciseness is becoming less challenging and more of a parameter as the field of additive manufacturing develops. Of more concern herein, metallic additive manufacturing powders and the powder stream which carries them are known to have efficiency of delivery to the additive melt zone less than that desired for more demanding applications.

Introducing electromagnetism to this thesis, when a straight electrical conductor of electricity has electrical current flowing in it, a magnetic field is present and is concentric to the wire longitudinal direction. If this wire is wound around a cylinder for shape, the individual turns of the wire act to modify the collective shape of this coil's magnetic field through superposition. Each turn of the coil acts to increase the magnitude of the field within the coil center as well as the field at the coil ends. An increase in current or an increase of turns or layers of turns in close proximity to an area of interest all act to increase the strength of the magnetic field generated there.

When an object that reacts to the presence of a magnetic field is introduced to it an electromagnetic force on the object becomes evident and that object then experiences motion according to Newton's laws if it is otherwise unconstrained. Thus a ferromagnetic particle in a powder stream entering the region of influence of an electromagnetic coil would have its path of motion affected particularly as it gets closer to the coil, where the forces from the magnetic field intensify according to the field strength.

Perhaps better known from the field of transformers or solenoids, electromagnetic coils are recognized for different characteristics depending on the applications in which they are required to perform. In additive manufacturing it is proposed that the shape of the melt pool and its density, and more importantly herein, an increase in the amount of ferromagnetic material in the melt pool region, often termed catchment efficiency or its improvement, can be achieved. This is proposed via the introduction of a magnetic field source beneath an additive manufacturing substrate with the ultimate

goal of improving this efficiency. Of most concern herein is the magnetic field present at the ends of such source.

1.1 Motivation

In industry and some academic settings, computer aided design (CAD) models are used to directly build three-dimensional objects using any one of several laser processes such as direct laser deposition (DLD) and selective laser melting (SLM). The increased shape, and geometric design flexibility possible with these additive manufacturing (AM) or 3D printing methods serves to promote their increasing popularity.

The typical powder deposition efficiency, from 25 to 45%, experienced has generated concern for those using laser techniques, even though undamaged powders have proven recyclable in some applications. However, when very high quality is required, such as in some aerospace applications, their re-use may not be practical. Surface finish may also be a concern and misdirected, semi-molten powder produced during the additive process may adhere to surfaces producing unwanted surface anomalies, [1].

With this in mind, the baseline motivation was to study how to improve catchment efficiency using electromagnetic and permanent magnetic solutions addressing the potential for a Gaussian distribution powder density increase, as a lensed focus created through particle path diversion.

1.2 Problem Statement

In AM processes, focusing of powder streams along the stream path has proven difficult using techniques other than those herein. Thus the re-directed attention herein involves concentrating on proximity to the stream target, the melt pool region, and incoming powder stream, from beneath the AM substrate material. In order to do this, a naturally constricting magnetic field presence generated beneath was required and the field from an iron core solenoid, or simply coil, was deemed suitable and later a permanent magnet substitute. The coil or permanent magnet north, or south, pole produces both radially inward, and downward force in relative proximity to this magnetic source. Figure 1.1: Magnetic field pole action, shows this with directed field lines but the action on a ferromagnetic is

always a drawing, towards either pole. Due to this, the side issue of choice of materials to use in any proposed experimental apparatus was necessitated towards non-ferromagnetics.

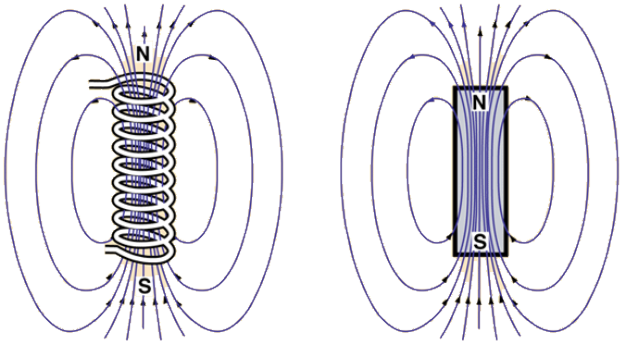

Figure 1.1: Magnetic field pole action, [2].

The issues addressed in this thesis involve presenting a novel way of proving the feasibility of such a construct to taper an AM powder stream in active proximity to either type of magnetic field source chosen, through analysis and simulations. A suggested experimental process regimen is also proposed.

1.3 Thesis Outline

The embodiment of this thesis is presented in eight chapters. Chapter 1 presents an introduction and discussion of the motivational issues and bolsters them through the sections continuance in providing the problem statement. Chapter 2 presents the initial approach taken, clarified through the presentation of introductory equations for catchment efficiency as background. It then provides the literature review conducted to critically provide information from sources available for developments in catchment efficiency improvement with an eye to manipulating particles in general. Relevant thesis content is also comparatively analyzed. Chapter 3 looks at the system design, detailing the principle elements involved in presenting a system overview, and the conceptual design describes their interaction. Process flows for the analysis, and simulation regimen are also presented and described. This chapter then closes with a free body diagram detailing the application of Newton's second law to a typical iron powder particle in motion in a magnetic field.

Chapter 4 looks at the lumped parameter model. First presented is magnetic field determination for an air core solenoid, on axis, then off axis with Biot-Savart in spherical coordinates. This is then adapted to comply using elliptic integrals in Cartesian coordinates for ease of manipulation and coding. Then further study through a set of summations completes this series. The results are compared through Matlab programming and plot comparisons using a benchmark example. Issues with the introduction of an iron core are outlined and then a ferromagnetic particle is introduced to develop model results for force. For this, magnetic field and magnetic field gradient equations are applied.

Chapter 5 continues these efforts through finite element modeling for the air core solenoid and iron core coil. The use of permanent magnets is introduced and studied. Processing of force generated parametric studies from the FEA software is described. Then post-processing in Matlab to generate particle displacement plots is also described. Chapter 6 gives information on additional and readily available magnet configurations simulated and provides iron particle trajectory plots. Chapter 6 ends with introduction of proposed experimental studies provided in Appendix F.

No experimental results are given as this is left to future work as outlined in Chapter 7 where conclusions are also presented.

Chapter 2
Background and Literature Review

In this chapter, catchment efficiency and how it relates to powder particulate path diversion in AM is introduced. Also, the subject of electromagnetism is described and how the two relate, and are considered in conjunction. Powder stream intensity distributions are also introduced, leading into a definition of catchment efficiency relevance with descriptive equations. This closes the background, and leads into the literature review which actively describes the state of the art of particle path diversion as it relates to particle manipulation methods, in general. The chapter closes with further clarification of the relevance of catchment efficiency, and a lead in to matters surrounding the magnetic fields, spatial derivatives, and forces involved. Also, published theory insights, and the dynamics involved with path diversion are presented.

First, some background on the subject of additive manufacturing (AM) is provided.

2.1 Background

Additive manufacturing (AM) is becoming more in-demand, sometimes bringing it to a level of equal or greater consideration when the alternative conventional solid-block subtractive manufacturing, and other manufacturing methods, fail to provide an adequate solution for parts formation. In AM, intricate and complex geometry can be created as the part is slowly built up from nothing, usually in a stratified layer-by-layer manner, as opposed to subtractive where the part is machined from a solid block, removing material as the formation process progresses. In AM, when metallic powders are used, the AM system delivers powder using a shielding gas, to transport it to the build zone. The amount of powder which is amalgamated in this melt zone, through laser activity, is typically much less than that delivered by the powder spray in its entirety. The relationship between these is often considered to be what is termed catchment efficiency, a ratio of them, expressed as a percentage, or a ratio of spray contents reaching the melt zone to the total amount of spray delivered.

In electromagnetism, magnetic fields can be generated that act on a ferromagnetic particle in their vicinity. Introducing a field to a metallic powder stream in AM has the possibility of the field lines acting on a ferromagnetic particle entering the field, and redirecting it, such that its path of travel has

it entering the melt pool when it otherwise would not (in the absence of such a field). The goal herein is to use an electromagnetic source, a coil, or solenoid, replaced by a strong permanent magnet, or magnet configuration, for simulation, producing a similar magnetic field, to alter the path of a ferromagnetic particle when it is within relative proximity to this magnetic field construct. This would help to improve the amount of metallic powder directed to the melt zone and increase the ratio mentioned, thereby improving catchment efficiency. The focus herein is the analytical and simulation sides of redirecting a particle with the use of such a field, in a feasibility study. The field source is to be placed beneath the AM substrate material, coaxial to the melt zone, with the powder stream completely vertical, and the field construct also axially vertical, as a proof of concept, as well as feasibility study.

Figure 2.1 shows a representative vertical powder nozzle and powder distribution intensities at various elevations. Of interest here is the potential for a localized constriction of the intensity at a specific elevation relative to the substrate to effectively increase the amount of powder that is incident and part of the melt pool.

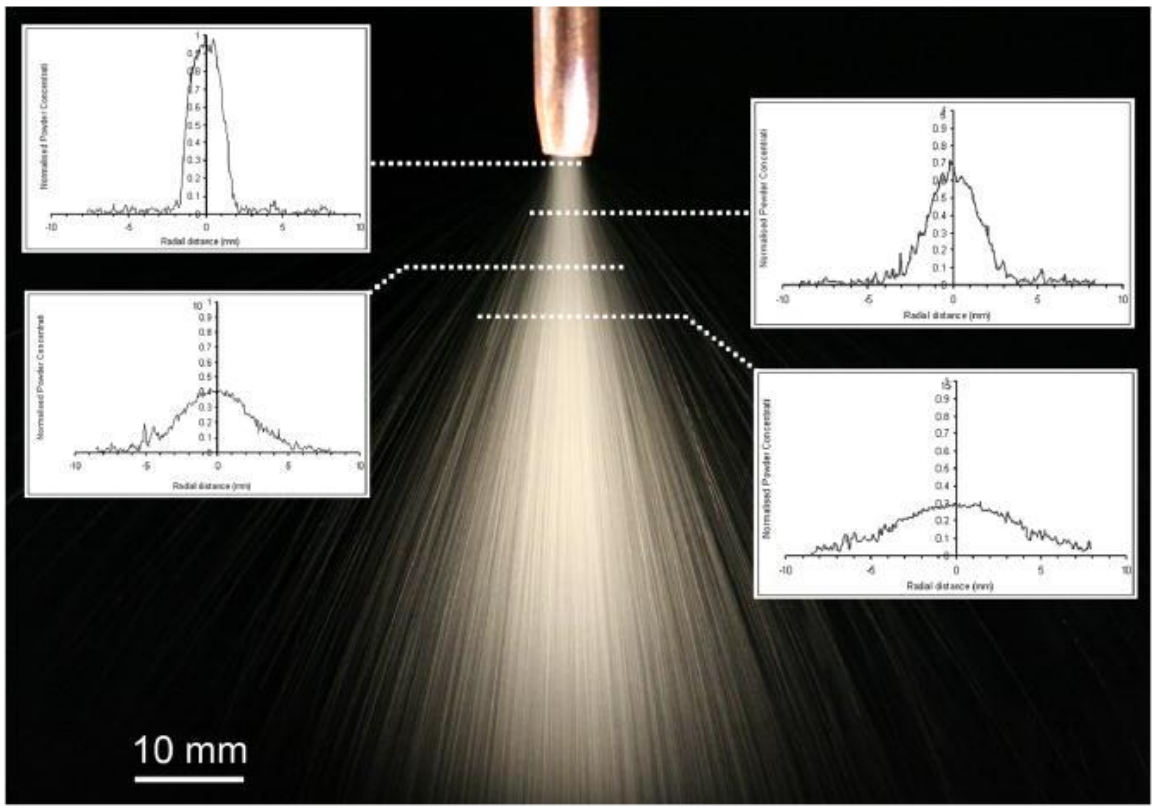

Figure 2.1: Vertical powder stream intensity elevations, [3].

Presented next is a description of the mathematical representation of catchment efficiency used as a guide in portraying how the intensity increase can be used to improve it.

2.2 Relevance Definition

Catchment efficiency is often presented in studies, but its improvement is rarely a focus. One cannot say it is a growing aspect of the AM field, but its presence is definite and is perhaps best described as a developing concern. It is typically reported as a percentage, either a ratio of metrics, or a ratio of effective to total powder particulate area concentrations.

The state of the industry in this regard appears to be focused on two catchment efficiency models. The first involves a ratio of the product of the clad area as a vertical cross section of the powder melt, the scanning (traverse) speed, and powder density, to powder feed (mass flow) rate. The equation is presented below, ([1], [4], and [5]), as (2.1).

$$P_e = \frac{A_c S \rho}{F} \; and/or, y = \frac{A \rho v}{m'} \tag{2.1}$$

In this equation, P_e, y represent catchment efficiency, A_c, A represent area of the clad (vertical cross section of the powder melt) as shown in Figure 2.2, S, v are the scanning (traverse) speed, ρ is powder material density, and F, m' are the powder feed rate as a mass flow.

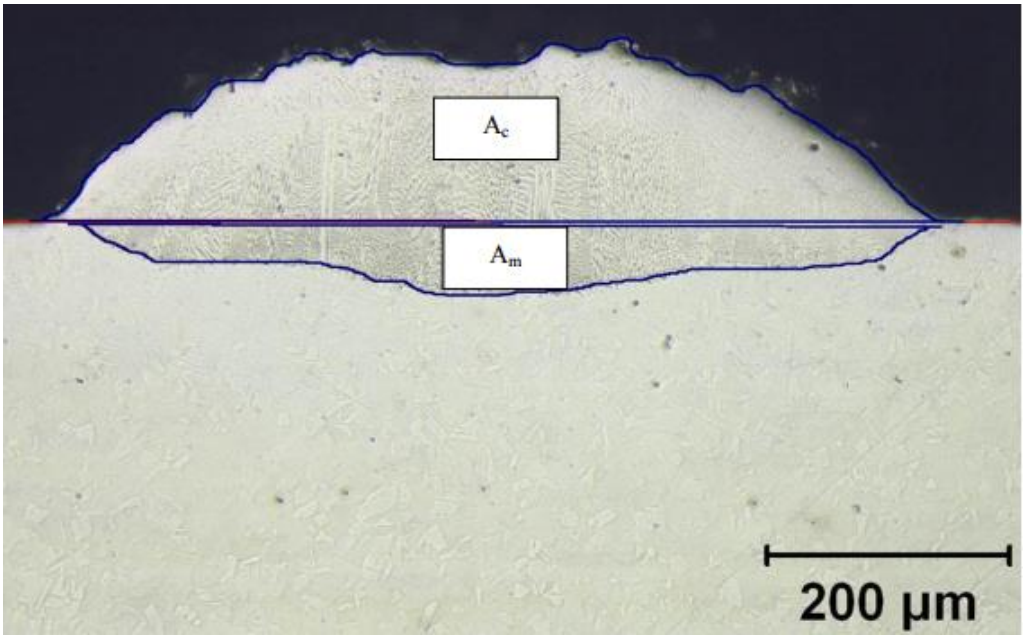

Figure 2.2: Micrograph showing molten area (A_m) and clad area (A_c), [5].

The second model involves the ratio of the molten pool area to the jet area on the substrate and notably increases with an increase in laser power ([6], [7]). It is presented in equation form, below.

$$\eta = \frac{S_{jet}^{liq}}{S_{jet}} \; and \; \eta_p = \frac{A_{jet}^{melt}}{A_{jet}} \tag{2.2}$$

In this equation, η, η_p represent catchment efficiency, or powder efficiency, $S_{jet}^{liq}, A_{jet}^{melt}$ represent the molten pool area as shown in Figure 2.3, and S_{jet}, A_{jet} are the substrate area impinged by the powder jet.

Figure 2.3: Molten pool and jet area, [6]

Either of these equations can be used to represent catchment efficiency improvements but the studies undertaken herein did not involve dynamic or static jet or melt pool geometry determinations. With other factors such as laser power, scanning speed, and powder feed rate held constant, the focusing of the powder stream due to the introduction of electromagnetic or magnetic fields was anticipated to prove readily observable.

Other descriptors for efficiency introduce the powder stream as a distribution that is Gaussian. The tightening or lensing of such a distribution should serve to produce a taller, more centralized three-dimensional spread with central, axial mean and smaller, concentric standard deviation as alluded to in Figure 2.1.

The focus of the study undertaken is on theoretically increasing the clad area in the first equation within the translational region of interest, with traverse speed constant. This is the choice for model development guidance and is the governing protocol. A powder consisting of iron (ferromagnetic) particles was central to the study and a single powder grain is considered.

The next section focuses on the state of the art as presented from a search of relevant materials using online methods via a literature review.

2.3 Literature Review: State of the Art

Additive manufacturing has become a mainstay as a manufacturing process and improvement of catchment efficiency is becoming a growing concern. There are several references to it and related items in the literature. Attempts at path diversion, and ferromagnetic particle path diversion, are

somewhat scarce. Nonetheless, the following is presented as a review of the available literature regarding manipulating particles in general, as well as ferromagnetics, and represents a sampling of what may be available in complete.

Simply changing the gas flow rate to provide less dispersion in the powder stream exiting the stream nozzle acts to reduce the overall powder feed rate in the denominator of equation (2.1), ([1], [4], [5]), alluding to increased efficiency. Although this decreases the mass flow rate, the substrate traversing speed would then need to be decreased, logically leading to adverse changes in the thermal (laser) parameters. A balance of these three elements would be required through the establishment of parameter sets. Alternatively, simply increasing the number of powder delivery nozzle systems, with multiple nozzles and multiple powder streams, would increase the amount of powder getting to the melt zone, but would not address the catchment efficiency concerns for which particulate path diversion is herein tantamount.

Provided in [8] is a mathematical model for catchment efficiency, but it does not allude to its improvement. It is simply stated as a ratio of mass of powder particles falling into the molten pool to the mass of powder particles stored in a specified cylindrically bounded powder flow field. Whereas provided in [9], is a method to increase efficiency by modifying the nozzle of the powder delivery system, targeting usability in industry. Within, catchment efficiency is defined as the mass of the clad layer(s) to mass of the powder ejected from the nozzle(s). But nozzle design is not of concern, herein.

An aerodynamic beam generator for large particles is described in [10]. Velocities are in the few feet per second to supersonic range dependent on the conditions of operation and configuration chosen. The generator is patented, and it can be used to produce a tightly focused beam of particles only described as large, also not of concern herein. In contrast, [11] uses efforts directed at increasing the powder deposition rate instead of analytical efficiencies by using multiple laser beams and powder nozzles to deliver more material to the additive zone(s) per unit time. Features of the object to be created are outlined by a single laser and featureless regions are then filled in using a series of laser beams which are equally spaced to complete, allowing fabrication time to be greatly decreased. This also does not properly address the concerns herein as multiple lasers are not considered.

Eddy current manipulation is used in structural integrity of components in non-destructive testing and for separation of electrically conductive materials in waste streams where management of

particles with dimensions on the order of five millimeters and less is possible. The manipulation process uses a rotor to create an electrical torque field introducing spin in order to elevate the particles to a stream removal height [12]. As the particles used in the analysis and simulations of this thesis are assumed to be spherical and uniform in density, the introduction of spin through electrically induced torque would be difficult. In actual fact the additive manufacturing particles are not typically perfect in this manner, and could possibly be processed in such a way. Further, use of a fast spinning magnet has also proven effective in manipulation of ferrous/non-ferrous mixtures with the non-ferrous particles tending to jump when they pass over the magnet. This is due to the repulsive Lorentz force, which allows particles that reach a certain height to be collected. However, eddy currents are easily produced in metals which have a high electrical conductivity to mass density ratio and iron does not, making the use of eddy current techniques here a very difficult method to achieve success with. Further, a high frequency eddy current source operating in the 100 kHz range is typically adequate for particles of 200 microns and up [13] making it further impractical for use herein where maximum particle size is about 125 microns.

Additionally, introduced in [14], a ramped configuration eddy current system using permanent magnets to deflect non-ferrous metallic particles describes a separation process. But it additionally states that ferrous (deemed magnetic) metals need to be removed from the stream as they would simply adhere to the permanent magnets, also somewhat a concern herein. This would block the stream and impede proper operation of the eddy current system. A similar rotary configuration is presented in [15].

Particle manipulations are studied in [16] using electrodynamic separation to impart momentum in a pulsed magnetic field. It involves using cylindrical particles with their symmetry axis along the magnetic induction vector. Again, particles studied herein are assumed spherical with uniform density making the content of [16] not completely applicable.

Efforts at Boeing have recently centered on magnetic levitation effects to create additive manufacturing constructs. The nugget created involves super-cooling turning it into a superconductor, for which the additive material becomes diamagnetic. Levitation relieves the nugget of the requirement for a supporting platform during the build [17]. The process is very costly and structural integrity involving internal stresses is driven by the inherent temperature range. The part is also fragile, susceptible to shatter fracture at the low temperatures involved. In contrast, [18] introduces electromagnetic levitation melting using eddy currents. Special equipment to produce both

electrostatic and electromagnetic levitation is required, wherein each is typically dependent on the magnetic source strength and frequency. The costs involved make this impractical herein.

The theory involving charged particles in motion becomes applicable for electrons or heavy ions and is limited by the static field electrical breakdown of 10^7 V/m. Also, the magnetic forces generated on these charged particles are much smaller than the electrical forces [19], [20]. The particles studied herein are charge neutral.

Steering of a ferromagnetic particle along a predefined path in a fluidic environment is introduced in [21] (and several of its listed references). Here, a MIMO system is described, built on previous knowledge regarding a SISO finite-dimensional nonlinear system. Helmholtz coils and an MRI environment are assumed with the focus on controller model development, for biomedical applications. State space representations are used for particle guidance systems whereas the content of this thesis is not controller based, but substantiates particle deflections in a constant magnetic field as opposed to particle path planning and confirmation.

Introduced and described in [22] is transfer efficiency, melting efficiency, and deposition efficiency, the last of which is of concern here. It is "used to describe the ratio of actual deposition rate (i.e., powder that is fused into the melt pool) to the total mass flow rate of powder delivered by the system." Here efficiency is described mathematically with an equation similar to (2.1). Efficiency was quoted within at a maximum of fourteen percent due to the fact that most of the powder delivered never comes into contact with the melt pool. A pair of semi-empirical equations is developed relating the three efficiencies through regression analysis of ln-ln plotting. This depth of interpretation was not considered applicable or necessary for the processes herein.

2.3.1 Catchment Efficiency Declared

Returning to the opening equation pair of section 2.1 from [1], [4], and [5], powder efficiency is presented as the ratio of clad area multiplied with traverse speed and powder density, to the powder mass flow rate. Although the bulk of these three literature items contents is not appropriate for the type of AM anticipated in this thesis, the equation used for catchment efficiency is inherently applicable and relevant as an adequate descriptor. The fact that area of the clad (melt pool section) is part of the numerator definitively shows that increasing this variable directly increases efficiency and this acted to provide inspiration for the efforts within this thesis.

The nine exogenous process parameters with direct effect further studied within [1] included laser power, laser beam diameter, scanning speed, powder particle size, and powder delivery rate, powder carrying gas flow rate, powder delivery nozzle diameter, its offset distance, and angle. In this thesis, all of these were established to be held relatively constant for proposed experiments. But the second equation of the first pair given in section 2.1 for y contained within [1] is relevant for the reasons just stated in the close of the previous paragraph.

The second equation pair of section 2.1, from [6], and [7], uses a different expression for powder efficiency based on a horizontal area ratio of melt surface to powder stream surface. Relevancy of these expressions to this thesis approach is minimal as they contain no direct reference to bulk clad sectional area. However, if the powder stream surface area were to be shown as decreased under action of the presence of the introduced magnetic field to the point where the entire stream were within the laser zone, although not practical, their relevancy would be confirmed.

Introduction of a Gaussian powder catchment efficiency function shape in [23] shows a potential method for determination of powder distribution. Here it was assumed that powder intensities would be measurable and presentable as such if additional study were done. The stream would be photographed and with the processed photo file, would have powder density confirmed via intensity of stream portions as sectioned within the photograph of Figure 2.1.

2.3.2 Magnetic Fields, Spatial Derivatives, and Force

Herein, four approaches from the literature were studied and undertaken in progression. The process started with the **B** field on the central air core solenoid axis in [24], with programming in Matlab and modelling in COMSOL Multi Physics. Here, the analysis also included coil replacement with a permanent magnet.

Next, the consideration of the magnetic field off axis for a circular current loop was studied as in [24] in the x-y plane producing a result in spherical coordinates. The conversion of this to Cartesian coordinates involved the evaluation of elliptic integrals. Rather than evaluate approximately using an expansion series numerically, the set of expressions in [25] from the law of Biot-Savart involving complete elliptic integrals of the first and second kind were used. This allowed for easy programming for magnetic field calculations at an off-axis (any) point in space using Matlab. The code was readily developed for multi-turn, multi-layer solenoid **B** field component magnitudes as well.

As a second process for comparison purposes using a benchmark example from [26], code in Visual Basic from this source was adapted to Matlab. It was shown to be in agreement with the results from the process involving [25], as well as the given benchmark (of subsection 4.1.5) results. The process of [26] involved a set of summation equations in Cartesian coordinates for a precision result developed based on choice of angle increment in the discrete, summation equations.

In the category of general physics, equations developed for the components of the magnetic field for a single current loop in [27], in agreement with those described above were used as confirmation for those of [25]. This source, [27], also provided their spatial derivatives with all presented in spherical, Cartesian, and cylindrical coordinates. Of these, Cartesian proved very useful for programming for magnetic field calculations as well as force on a particle calculations, adaptable for multiple turn, multiple layer coils.

Expressions for the analytic representation of the force on a magnetized object were used as provided in [28]. Along with expressions for magnetization and the spatial derivatives from [27], the components of the force on a particle in a magnetic field could be calculated. Portions of the content of [29] provided virtually identical equations for force as developed in [28] with the exception that they were expressed in terms of magnetic field intensity, **H**, in place of magnetic flux density, **B**. Applicability of the equations from [28] and [29] is further confirmed in the literature in [30] where they are carried forward, as used in abrasive application, to magnetically induced cutting particles, not relevant in this thesis.

2.3.3 Published Theory Insights, Dynamics, and Path Diversion

The equations and content of [31] served to introduce the writer to the field of electromagnetics and the relevant theory surrounding implementation of Maxwell's equations, in particular, the divergence and curl of **B**. The theory in [31] was extended in [32] and was consulted for additional background on relevant theory regarding magnetic fields and force calculations.

Further clarification of the relationship of magnetic field, **B**, to magnetic field intensity, **H**, and further, magnetization, **M** was given by [33]. These relationships greatly assisted with the calculation of force on a particle in a magnetic field and although obtained as an early reference proved to advance the transparency of this knowledge later in its development. This reference was further

consulted when basic knowledge was required, providing necessary background information, inclusive of Maxwell's equations, for example.

The content of [34] served as an introduction to some of the terminology surrounding laser additive manufacturing. It provided a general outline for relevant stages of the writer's thesis direction and segmentation with areas such as research of existing documentations and publications, analytical studies, simulations, and proposed experiments. It further served as a ready reference for lexicon and was a periodic source for clarifications.

Magnetic levitation of an iron ball, as described in [35], served as an introduction, possibly adaptable to an iron particle. An iron ball was encased in a plastic box and attempts were made to have the ball float in mid-air. Although not directly related to the processes studied in this thesis it does serve to provide a general concept to apply such as the redirecting of small iron particles upon which this thesis is based.

The content of [36] was consulted for its writings on fine particulate dynamic motion and the aerodynamic forces which ensue. After careful consideration its informative material was disregarded as gravity forces on the iron particles were deemed negligible. Further, due to the small frontal area of the particles, drag forces were also considered negligible. Even still, these forces were included in the processing and solving of the differential equations of section 5.4: Post-Processing in Matlab.

The content of [37] presents a method of determining the catchment efficiency by taking the average of the double integration of a probability density function over two area representations of portions of the melt pool. Further relevant content includes processed images of powder streams showing grayscale intensities as definitively Gaussian similar to Figure 2.1. Although the material presented within is tantamount in its detail to catchment efficiency, only some of the writings within were directly aligned with the content and direction of this thesis.

Chapter 3
System Design

In this chapter, a general overview of the AM process in the vicinity of the region of interest where the active clad would be located is presented. Also, the guiding paradigm with regard to materials, process, and suggested method for confirmation is given under Conceptual Design Justification. The process flow elements are stated. Analysis and simulation flow charts are provided and described. Lastly, Newton's second law is applied to an iron particle with a free body diagram presented in Figure 3.5.

3.1 System Overview

Central to the studies is the iron powder that would be used for the AM process. Stainless steel containing a seventy percent content of iron by weight was considered. For ease of analysis and simulation pure iron was decided upon, for simplicity, and also for the fact that one hundred percent of its content is ferromagnetic. This would ensure a stronger path diversion of the powder under the force introduced with the presence of the coil or permanent magnet's magnetic field.

An argon delivery and shielding gas would deliver the powder at a rate of two meters per second to the active zone. The argon, being inert, shields the laser activity as in a welding process, ensuring no impurities develop. The shielding is temporary. Once the active zone propagates as the substrate undergoes translational motion with the stream stationary and constant, the weldment surface is free to oxidize. More importantly, the internal geometry of the clad would remain purely as intended to ensure its needed mechanical properties. It is important to note that although the gas used is in fact very much needed as shielding during laser activity, the principal suggested verification process uses the gas purely on the basis of its particle stream delivery ability.

A substrate was to be used and its elevation would be constant, with no translation in the analytical y-direction and motion purely in the analytical x-direction. Figure 3.1 shows the basic system used in a two-dimensional figure. The powder delivery nozzle and permanent magnet configuration remains stationary while the substrate translates horizontally in the x-direction shown.

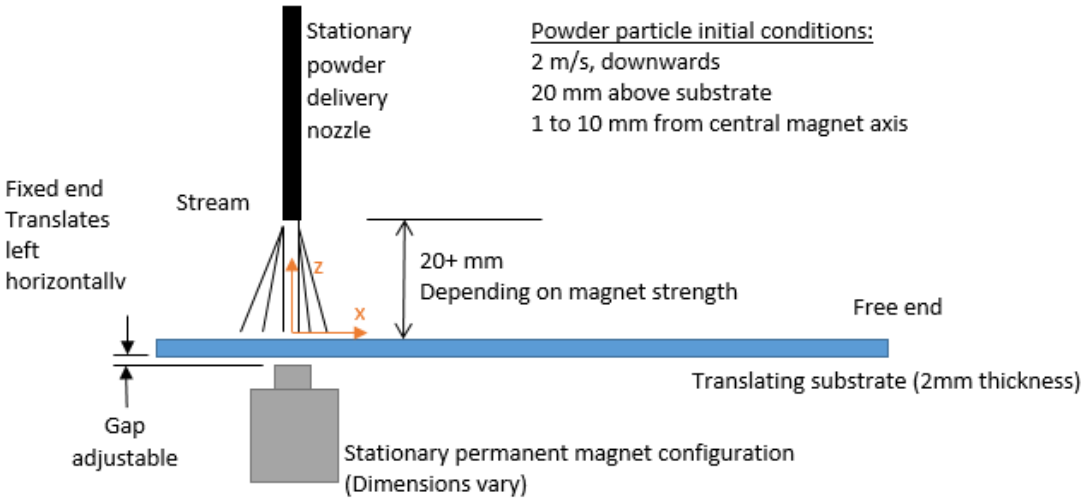

Figure 3.1: Basic system components

Considerations regarding the conceptual design are presented next.

3.2 Conceptual Design Justification

Choice of substrate material was first suggested as steel or aluminum, with aluminum being the logical choice. Although the steel would work well preliminarily to show the powder stream in its unaltered path, when the magnetic source was brought in proximity to this material it would immediately be drawn to it. This would make the apparatus very difficult to assemble, and future prototypes to operate. After additional research, it was determined that the aluminum, although non-ferromagnetic, possesses heat transfer characteristics which are much greater than steel. If welded with the laser equipment available it would simply melt the aluminum substrate through thickness completely, locally. A more practical, but more expensive alternative was suggested as titanium. It has close to the same heat transfer abilities of steel for which the available equipment laser parameters were already known, and, it is non-ferromagnetic. This would all become relevant if the experiments proposed involved laser operation.

Propagation of the substrate through translational motion during the proposed SLM activity was to be in the y-direction of the CNC apparatus (analytical x-direction). If the laser were to be working,

the powder delivery nozzle would be angled, to avoid interference, as the laser line-of-sight is purely vertical. If not working the nozzle would be purely vertical.

It is notable that there are issues anticipated with powder attraction to the magnetic source of choice as the substrate translates. An accumulation of powder may be dragged along the substrate surface. This may possibly be accommodated through quick acquisition of photographic evidence of stream constriction as soon as the process of powder delivery commenced.

The preferred orientation of the powder delivery nozzle for simplicity herein is purely vertical. This would allow the magnet to be aligned with the powder stream central axis providing an un-skewed, concentric particle intensity distribution. It would potentially then be observable as a tapering, or constriction of the stream in proximity to the magnetic source. This is in contrast to the purely concentric shaped right conical form which is present in the absence of a magnetic field source.

The balance of the process would involve simply obtaining photographic evidence. This would validate the process, showing a powder stream tapering when pictures with and without a magnetic field source present beneath the substrate as it translates are taken and compared. The use of appropriate photography equipment, lighting and special conditions such as choice of backdrop would reveal this.

Process flow for the two research segments of analysis and simulation is presented next.

3.3 Process Flow

The approach taken herein involved establishment of the initial conditions for a typical ferromagnetic particle, followed by analysis of forces established from the particle being present in a magnetic field. Then simulations were undertaken in the FEA software, with the last logical step being experimentation (left to future work) to validate results of the simulations and analysis. The structure of the relation of these is as presented in Figure 3.2.

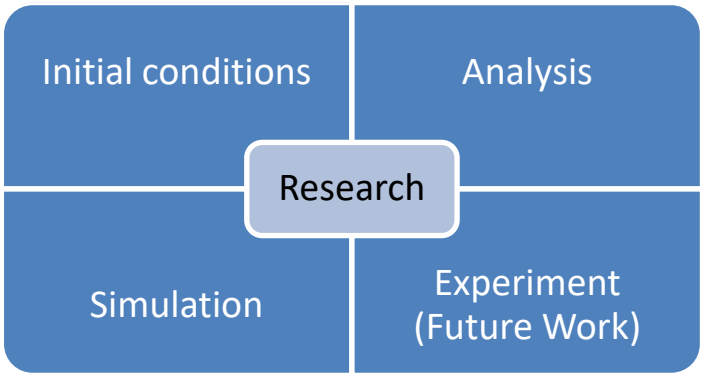

Figure 3.2: Process flow elements

The first of these, analysis flow, is presented next.

3.3.1 Analysis Flow

The originally intended analytical method began with establishment of the ferromagnetic particle initial conditions. These were taken with respect to position relative to the central core of the magnetic source (x-direction (1 to 10 mm)) and top of substrate (z-direction, 20 mm, above)), and the powder stream nozzle exit velocity components ($v_x = 0$, $v_z = 2$ m/s, downwards). Next, Matlab was to be used to determine the magnetic field components. A meshgrid was used to generate a 1mm resolution lookup table. Then the particle was to be introduced, and force calculations on the grid were to be calculated, also in Matlab.

From here, the ode45 function of Matlab and double interpolation of the force component lookup tables were to be used to determine particle positional data. Lastly, the particle positional data from the differential equation results array was to be plotted, also in Matlab. Figure 3.3 shows a process flow for this procedure.

It is notable that this complete analytical model was not sufficient to describe the magnetic field and force data adequately. This is further noted in section 4.1.9, leading to the assumption that the FEA method involving COMSOL Multi-Physics superseded the analytical process, with further study of the analytics involved left to future work.

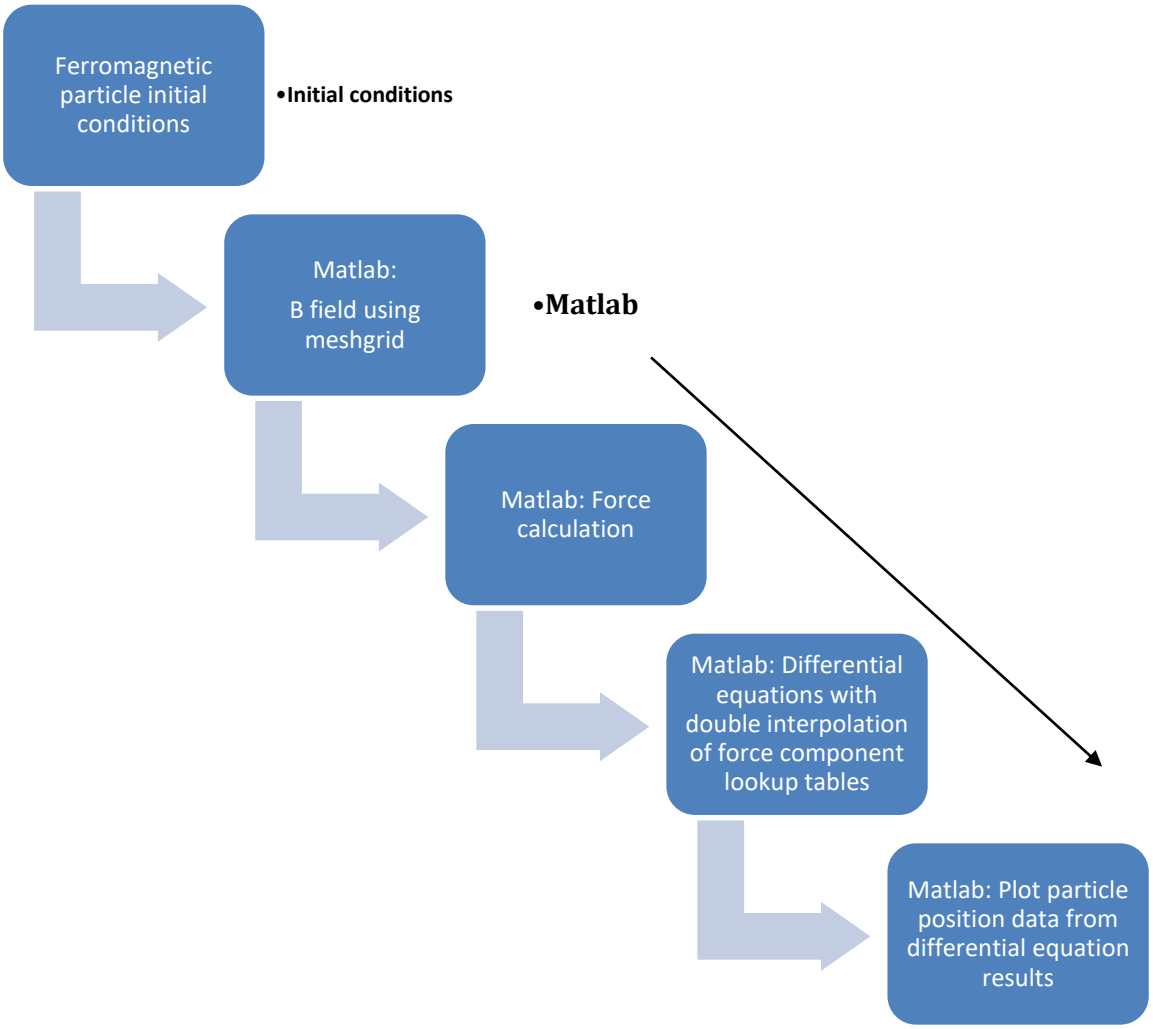

Figure 3.3: Originally intended analytical process

Next, simulation flow is described with the addition of finite element analysis.

3.3.2 Simulation Flow

The simulation study began with modeling of the magnetic source in COMSOL Multi-Physics. Once established, then the parametric sweep ranges were defined and the simulations begun. Upon run completions, force data could be generated and then formatted in MS Excel. These were established as .mat files in Matlab, where Matlab could then generate positional data using the initial particle

position and velocity conditions, the ode45 function, and the COMSOL lookup tables. Once the positional data was obtained, trajectory plots could then be created, also in Matlab. Figure 3.4 shows this process flow.

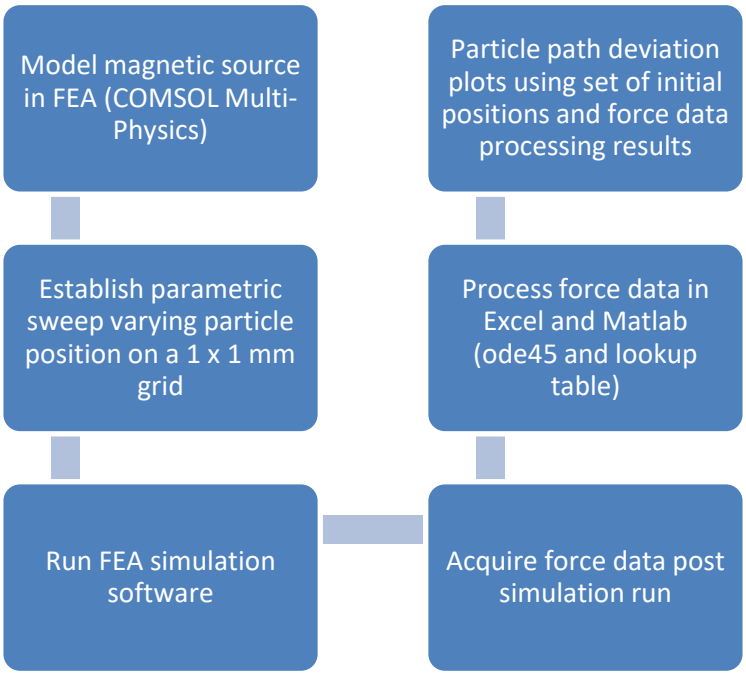

Figure 3.4: Simulation process

The next section provides details on the application of Newton's second law of motion to a particle in a magnetic field.

3.4 Forces on an Iron Particle

When an iron particle is in motion and is in the presence of a magnetic field, it is acted on by several forces as described herein. The forces to be considered include the magnetic force, aerodynamic drag force, and gravitational force. These are described here, in component form, with reference to Figure 3.5.

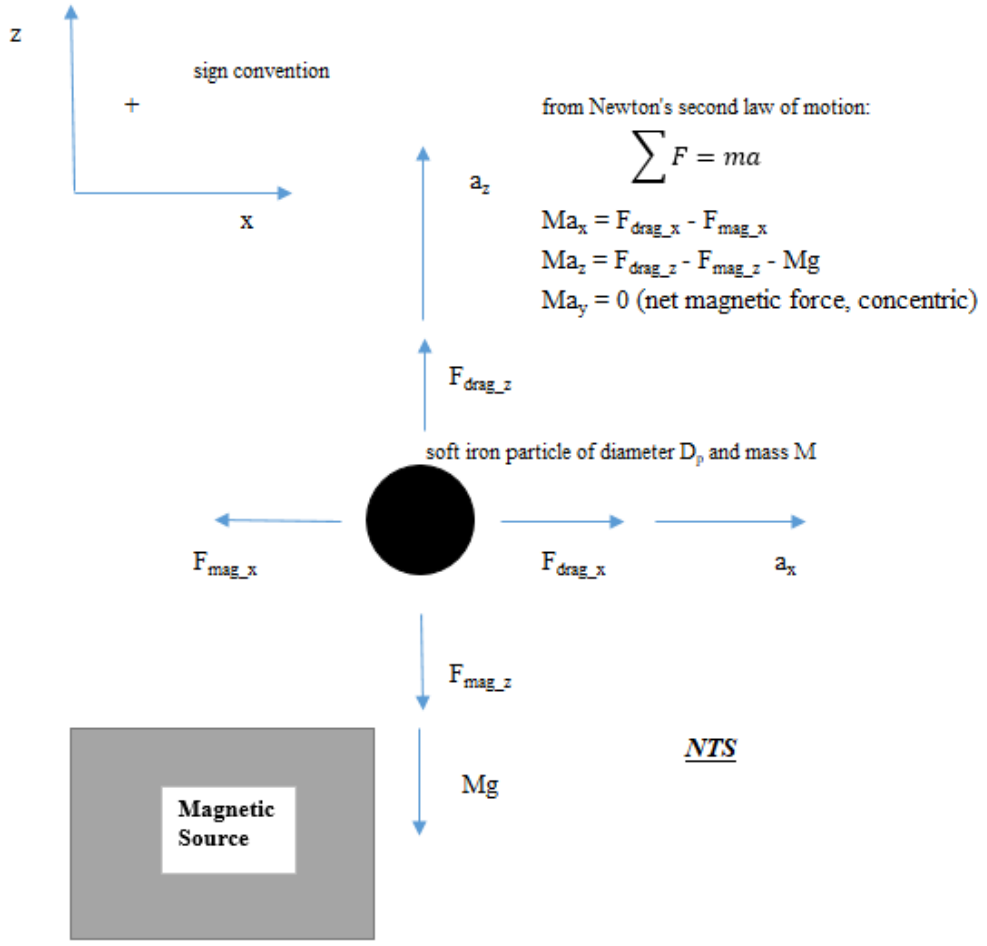

Figure 3.5: Newton's second law as applied to a soft iron particle in a magnetic field

From the vectors presented in Figure 3.5, and applying Newton's second law the sum of the force components in each direction of the Cartesian system are developed as follows.

$$\sum F_x = Ma_x = F_{drag_x} - F_{magnetic_x} \tag{3.1}$$

$$\sum F_z = Ma_z = F_{drag_z} - F_{magnetic_z} - Mg \tag{3.2}$$

$$\sum F_y = Ma_y = 0 \tag{3.3}$$

$$(as\ the\ analysis\ is\ planar\ with\ the\ magnetic\ force\ concentric\ in\ y)$$

In the use of (3.1) to (3.3), the magnetic force components developed are as presented in subsection 4.3.1 and Appendix E. Otherwise, they are obtained from COMSOL simulations in Chapter 5.

The gravitational force is determined from the mass of the particle based on its volume and density of 7800 kg/m^3. Lastly, the drag force components are developed from the Stoke's Law application of drag for a sphere in motion in a fluid, presented below.

$$Drag\ force = F_D = \frac{1}{2}\rho v^2 C_D A \tag{3.4}$$

In this equation, ϱ is the density of fluid taken to be argon (1.6339 kg/m^3 at 25 ºC and 14.696 psia), v is the velocity of the particle relative to the fluid, A is the frontal (cross sectional) area, and C_D is the drag coefficient, taken as 0.44, herein, for a sphere.

It is often taken that the drag forces are minimal as the AM particles are travelling with the argon fluid at a steady state velocity. However, herein they were included in the analyses to provide conservative results. The gravitational force developed is also significantly less than the magnetic forces involved due to the very small size of the particles involved, but once again was included for completeness, and a conservative result.

Chapter 4 next presents the lumped parameter model that was used for the analysis herein.

Chapter 4
Lumped Parameter Model

Chapter 4 content delivers a lumped parameter model. The approach herein was to first present introductory studies of the magnetic field calculation using four approaches for an air core solenoid including on axis calculations, off axis calculations, calculations using elliptic integrals, and lastly calculations using a set of discrete summation equations. A benchmark example is then used to proof Matlab coding and an introductory FEA model is presented.

Difficulties encountered with the introduction of an iron core to the benchmark air core solenoid are given. Also, a section on model results introduces force, and magnetic fields, with magnetic field gradients presented in Appendix E.

4.1 Air Core

The simplest representation for the analytical approach involved the breakout of the wire coil, free of substantial core material, in essence an air core solenoid (ACS). This reduced the number of materials present to one, just the coil of wire itself with the exception of air (the environment). This provided a system elegant in its simplicity, easy to analyze with knowledge readily available in the literature. Figure 4.1 shows an ACS and a planar portion of its field (actual field is concentrically revolved about central axis) used for analysis purposes.

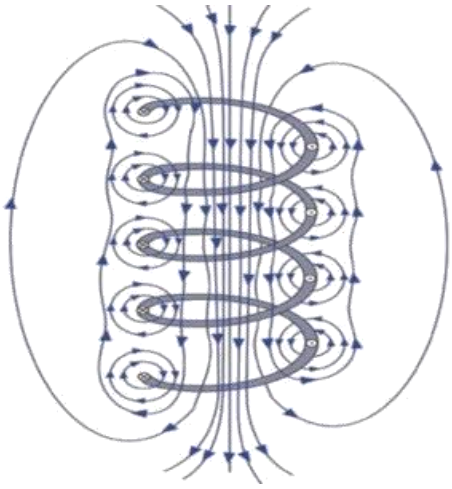

Figure 4.1: ACS, showing B field, [38].

The magnetic field on the central core axis is provided next.

4.1.1 On Axis

The central axis of the ACS along the core longitudinal axis was the source of analytical beginnings for determining the magnetic field strength. This focus allows first the magnetic field at a distance z, on the axis of a single loop of wire, with radius a, carrying a current of I to be presented ([24], from Biot-Savart), equation (4.1). Then this is adapted to a multiple turn, single layer set of stacked loops, Figure 4.3, as a very close approximation of the coil construct. The equations for this are presented as (4.2) to (4.5), below. Also, an image of the plot of the magnetic field for a representative coil with its parameters given in the title is presented in Figure 4.4. Take note that the **B** field is also symmetrically present for the other half of the coil as shown in the representation in Figure 4.1, not shown in Figure 4.4.

$$\bar{B} = \frac{\mu_0 I a^2}{2(a^2 + z^2)^{3/2}} \text{ for on axis} \qquad (4.1)$$

Figure 4.2 shows the reference geometry for (4.1).

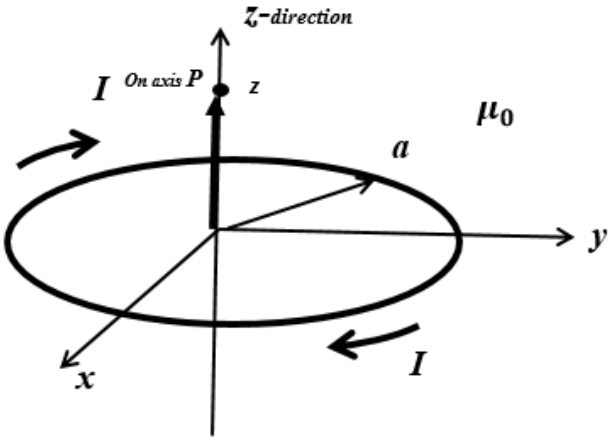

Figure 4.2: On axis reference geometry

(In the above μ_0, the permeability of free space $is\ 4\pi \times 10^{-7}\ Hm^{-1}$).

For the single layer solenoid of length *l*, with *N* turns developed similarly to that in [24], from Biot-Savart, using a multi-turn coil simplified to a stacked set of loops:

$$d\bar{B} = \hat{z}\frac{\mu_0 \frac{NI}{l} a^2}{2[a^2 + (z - z')^2]^{3/2}} dz'. \tag{4.2}$$

Figure 4.3 shows the reference geometry for (4.2). In the figure, if we take a cross section of tightly packed loops at a height, z' having thickness, dz' the quantity of current flowing through them is proportional to the thickness of this cross section, given from the fact that $dI = I(\frac{N}{l})dz'$.

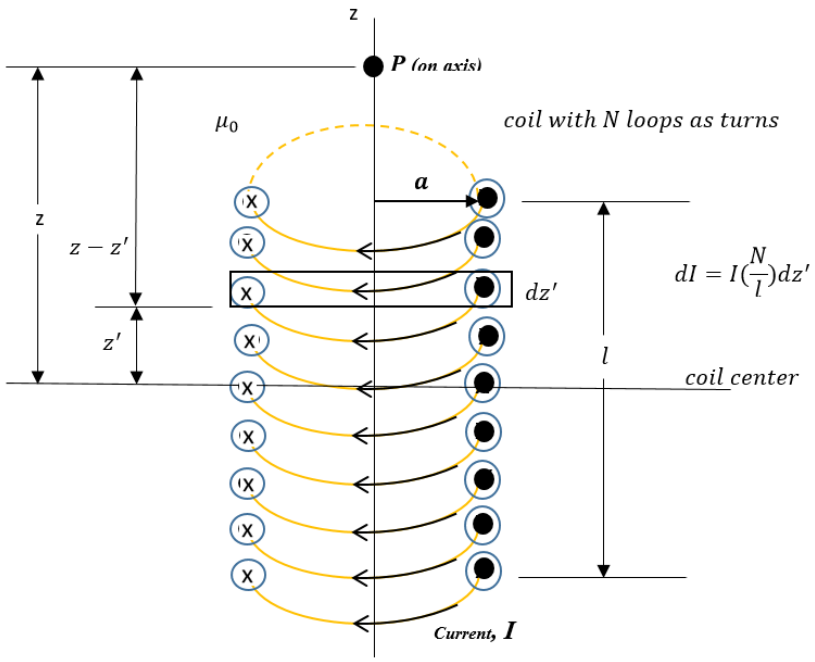

Figure 4.3: Multi-turn/loop coil (ACS), [24].

The integration proceeds as follows.

$$\bar{B} = \hat{z}\int_{-l/2}^{l/2} \frac{\mu_0 \frac{NI}{l} a^2}{2[a^2 + (z - z')^2]^{3/2}} dz' = \hat{z}\mu_0 \frac{NI}{2l} a^2 \int_{-l/2}^{l/2} \frac{dz'}{[a^2 + (z - z')^2]^{3/2}} \tag{4.3}$$

$$\text{By using } \int \frac{du}{(a^2 + u^2)^{3/2}} = \frac{1}{a^2}\frac{u}{\sqrt{a^2 + u^2}} \tag{4.4}$$

$$\bar{B} = \hat{z}\frac{\mu_0 NI}{2l}\left[\frac{z + l/2}{\sqrt{a^2 + (z + l/2)^2}} - \frac{z - l/2}{\sqrt{a^2 + (z - l/2)^2}}\right] \quad (4.5)$$

A plot of the magnetic field for a representative coil (top or bottom half of Figure 4.1) with its parameters given in its title is provided in Figure 4.4.

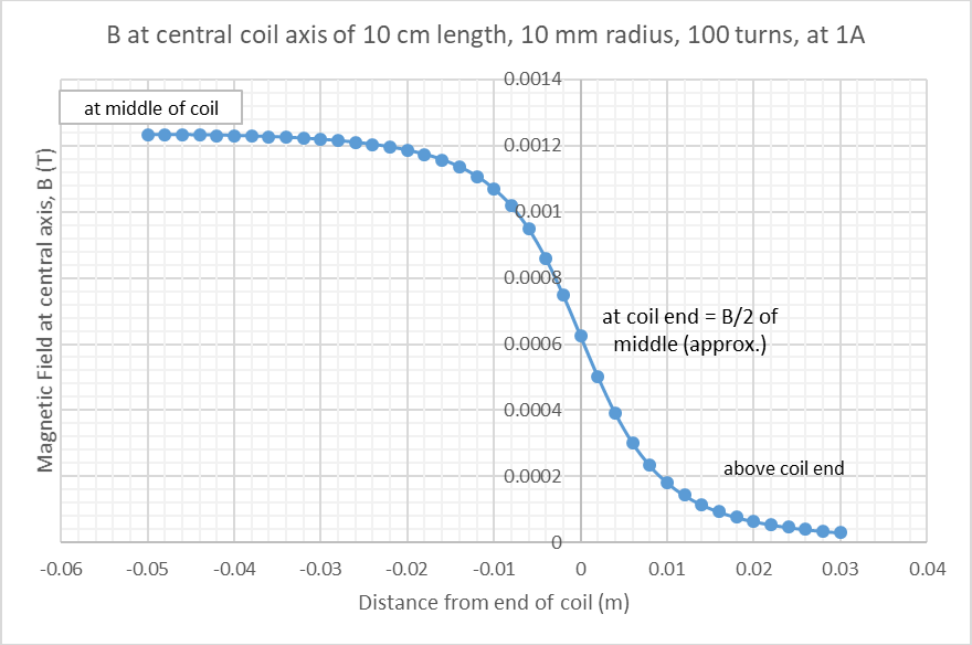

Figure 4.4: Magnetic field, B, along ACS central axis from coil center to 30mm above

From the above we can get the on axis magnetic field magnitude with direction along the axis.

Next, the magnetic field at a point off the central axis is considered.

4.1.2 Off Axis

On axis calculation of the magnetic field strength is adequate to introduce one to the expected shape and generally diminishing characteristics of the magnetic field with distance from the coil center and

its ends. For the purposes of this study, of more interest is the magnetic field off the central axis, or more precisely, anywhere in space relative to the coil.

The following figure, [24], shows a circular loop of radius R lying in the x-y plane and carrying a steady current I. The magnetic field at point P off the axis of symmetry is presented as approximations in Cartesian coordinates herein, with the following exact equations (developed in 9.8.19, 9.8.20, and 9.8.2, from the Appendix of [24]) in spherical coordinates.

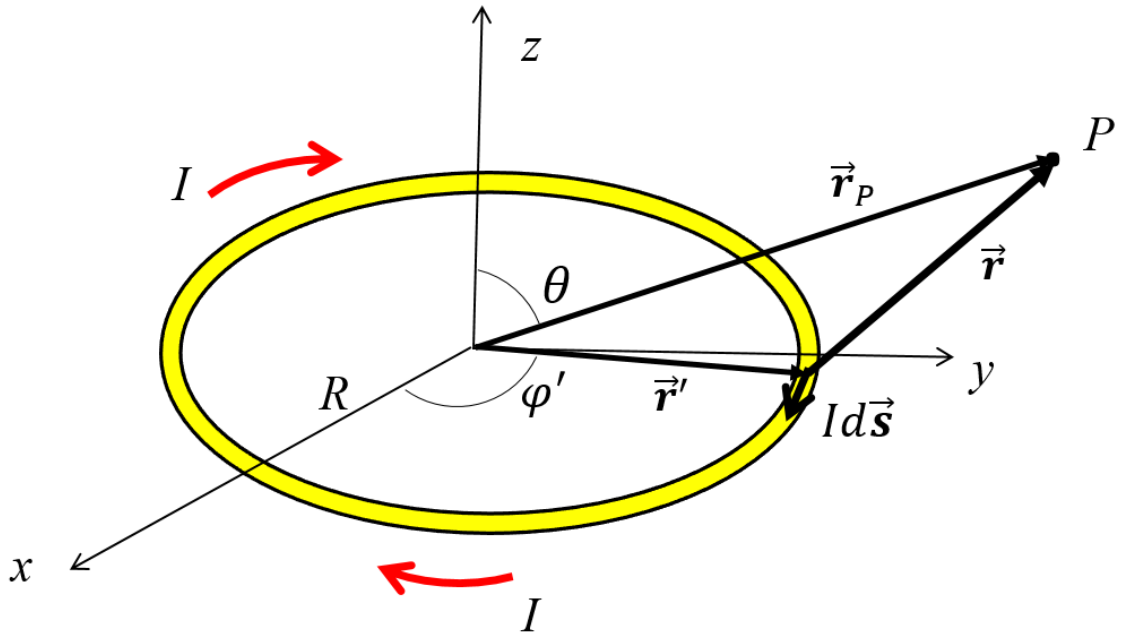

Figure 4.5: Single current loop magnetic field off the symmetry axis, [24].

$$B_r = \frac{\mu_0 I R^2 \cos\theta}{4\pi} \int_0^{2\pi} \frac{d\varphi'}{(R^2 + r^2 - 2rR\sin\theta\sin\varphi')^{3/2}} \tag{4.6}$$

$$B_\theta(r,\theta) = \frac{\mu_0 I R}{4\pi} \int_0^{2\pi} \frac{(r\sin\varphi' - R\sin\theta)d\varphi'}{(R^2 + r^2 - 2rR\sin\theta\sin\varphi')^{3/2}} \tag{4.7}$$

The variable r is defined as follows with θ and φ' as shown in Figure 4.5.

$$r = |\vec{r}| = \sqrt{(-R\cos\varphi')^2 + (y - R\sin\varphi')^2 + z^2} = \sqrt{R^2 + y^2 + z^2 - 2yR\sin\varphi'} \tag{4.8}$$

(In the above μ_0, the permeability of free space $is\ 4\pi \times 10^{-7}\ Hm^{-1}$).

The evaluation of these equations for given points in space involves the use of elliptic integrals, considered next, in order to produce more exact results.

4.1.3 Elliptic Integrals

Additional sources were consulted to attend to the presence of elliptic integrals with Figure 4.6 and equations (4.9) to (4.12) from [25]. The equations were verified through adaptation from a single current loop to that of a coil. The generated data was plotted for a benchmark example as outlined in subsection 4.1.7 and then compared to the supplied plots of the example from [26], shown in subsection 4.1.5.

Figure 4.6 was used for the following equation set.

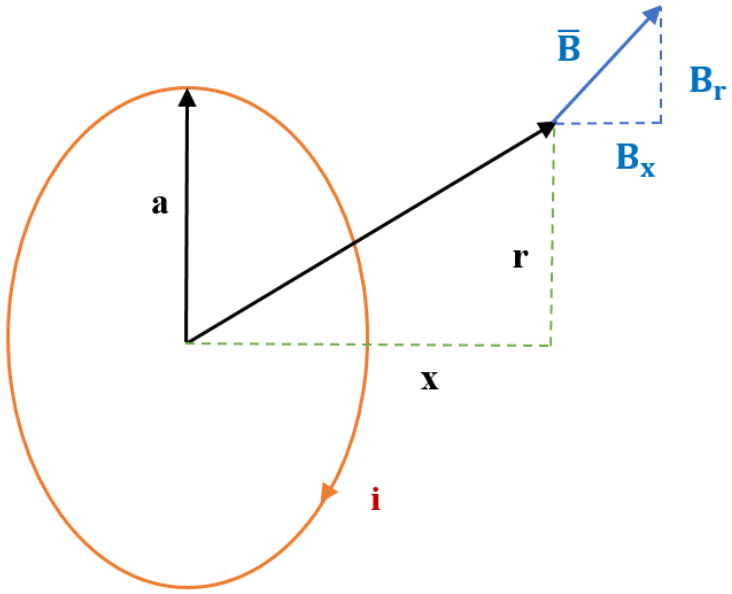

Figure 4.6: Single current loop for elliptic integral equations. Sum for all loops of solenoid by varying x and a as needed for each loop stacked both radially and longitudinally for close approximate of B components, [25].

$$B_x = B_0 \frac{1}{\pi\sqrt{Q}}\left[E(k^2)\frac{1-\alpha^2-\beta^2}{Q-4\alpha} + K(k^2)\right] \quad (4.9)$$

$$B_r = B_0 \frac{\gamma}{\pi\sqrt{Q}}\left[E(k^2)\frac{1+\alpha^2+\beta^2}{Q-4\alpha} - K(k^2)\right] \quad (4.10)$$

In (4.9) and (4.10), *B* is the magnetic field (Tesla) at any point in space that isn't on the current loop. It is equal to the vector sum of two field components, B_x, the field component that is aligned with the central axis, and B_r, the field component that is in a radial direction. The remaining variables are defined as shown in (4.11) and (4.12).

$$\alpha = \frac{r}{a} \text{ and } \beta = \frac{x}{a} \text{ and } \gamma = \frac{x}{r} \quad (4.11)$$

$$Q = [(1+\alpha)^2 + \beta^2] \text{ and } k = \sqrt{\frac{4\alpha}{Q}} \text{ and } B_0 = \frac{i\mu_0}{2a} \quad (4.12)$$

In (4.11) and (4.12), B_0 is the magnetic field at the center of the coil, *i* is the current in the loop wire (Amperes), *a* is the loop radius (meters), and μ_0 is the permeability constant (approx. 1.26 x 10^{-6} or exactly $4\pi \cdot 10^{-7}$ $H \cdot m^{-1}$ or $N \cdot A^{-2}$). Further, *x* is the distance in the axial direction from the center of the current loop to the field measurement point, and *r* is the distance in the radial direction from the axis of the current loop to the field measurement point. Lastly, $K(k^2)$ is the complete elliptic integral function, of the first kind, and $E(k^2)$ is the complete elliptic integral function, of the second kind.

From the above we can get the magnetic field magnitude in each direction.

An approximate representation is presented next, using a set of discrete summation equations.

4.1.4 Summations

The example benchmark from pages 7 and 8 of the online source at [26] uses the set of summation equations presented below, (4.13) to (4.15), as developed in [26]. Figure 4.7 is provided for clarity. The coil in the example is multi-layer and multi-turn in composition. The equations are presented as

describing the magnetic field in and around a finite cylindrical air-core solenoid. Similar to the elliptic, the proofing plots are provided in subsection 4.1.6, verified against those of subsection 4.1.5.

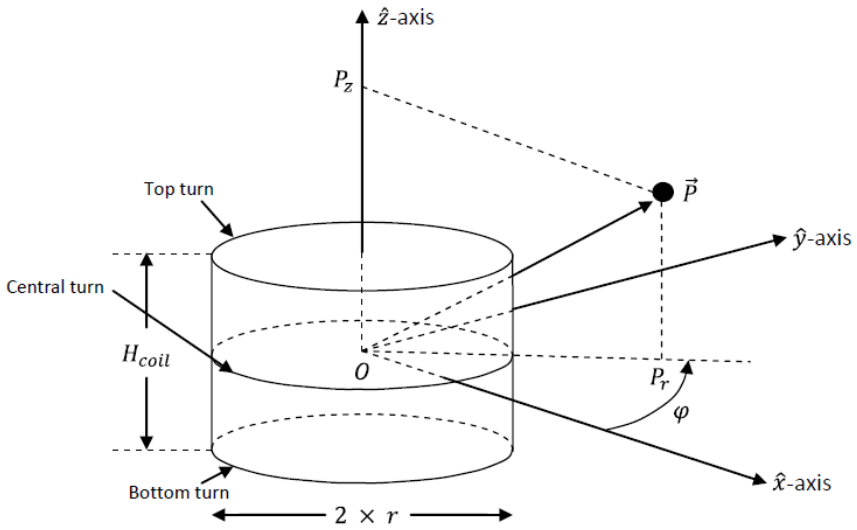

Figure 4.7: Air core solenoid geometry. For a radial cross section above the solenoid, assumed φ= 0 and $P_r = P_x$, [26].

The equations are presented, below.

$$B_x = \frac{\mu}{4\pi} \sum_{m=1}^{m=N_{layers}} \sum_{n=1}^{n=N_{turns}} \sum_{\theta=0}^{\theta=2\pi} \frac{I r_{Mth\ layer}(P_z - z_{Nth\ turn})\Delta\theta\cos\theta}{\left[P_r^2 + (P_z - z_{Nth\ turn})^2 + r_{Mth\ layer}^2 - 2P_r r_{Mth\ layer}\cos(\theta - \varphi)\right]^{3/2}} \tag{4.13}$$

$$B_y = \frac{\mu}{4\pi} \sum_{m=1}^{m=N_{layers}} \sum_{n=1}^{n=N_{turns}} \sum_{\theta=0}^{\theta=2\pi} \frac{I r_{Mth\ layer}(P_z - z_{Nth\ turn})\Delta\theta\sin\theta}{\left[P_r^2 + (P_z - z_{Nth\ turn})^2 + r_{Mth\ layer}^2 - 2P_r r_{Mth\ layer}\cos(\theta - \varphi)\right]^{3/2}} \tag{4.14}$$

$$B_z = \frac{\mu}{4\pi} \sum_{m=1}^{m=N_{layers}} \sum_{n=1}^{n=N_{turns}} \sum_{\theta=0}^{\theta=2\pi} \frac{-I r_{Mth\ layer}\left[P_r\cos(\theta - \varphi) - r_{Mth\ layer}\right]\Delta\theta}{\left[P_r^2 + (P_z - z_{Nth\ turn})^2 + r_{Mth\ layer}^2 - 2P_r r_{Mth\ layer}\cos(\theta - \varphi)\right]^{3/2}} \tag{4.15}$$

The variables in (4.13), (4.14), and (4.15) are defined with μ as the permeability of free space, I as the resident current, and r *as* the radius of the *Mth layer*. Further, z is the height of the *Nth turn*, P_z is the vertical coordinate of the point of interest, and P_r is the radial coordinate of the point of interest. Lastly, $\Delta\theta$ is the theta increment/division chosen to develop adequate accuracy (1000 increments proven), and φ is the angle from the x-z plane to the plane containing P_z and P_r.

The above equations can be used as an additional method to determine magnitudes of the magnetic field in each direction.

Next, the benchmark used to establish confirmation for analysis is presented.

4.1.5 Benchmark

The benchmark example used as quoted from page 7 of [26] is provided here:

> Example:
>
> Let us wind a coil using #28 gauge enameled copper wire. This wire has an outside diameter, including insulation, of 0.349mm and a resistance of 0.217Ω/m. A coil 100mm long will just accommodate 287 turns. Let the inner radius of the winding be 10mm and wind 16 layers. Finally, let us power the coil with 5V dc.
>
> The winding is 16 layers, or 5.584mm thick, so the average radius of all the turns is 12.792mm. The length of wire in the coil is the total number of turns multiplied by the average circumference, or 287 x 16 x 2 x π x $r_{average}$, or 369.1m. The resistance of the coil as a whole is 369.1m x 0.217Ω/m, or 80.1Ω. Ohm's Law gives the current through the coil as I = V/R = 5V/80.1Ω = 62.4mA.

The author then solves the summation equations to produce the following pair of plots used for proofing Matlab coding summation and elliptic efforts previously described, herein.

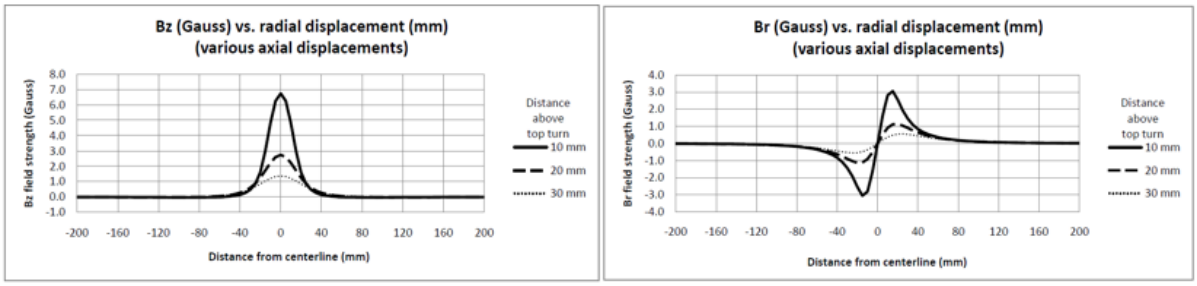

Figure 4.8: Vertical and radial magnetic field components for benchmark, [26].

The parameters of this benchmark are used in the following sections, 4.1.6: Summation Proofing, and 4.1.7: Elliptic Integral Proofing.

4.1.6 Summation Proofing

The following figure shows the plots obtained from adaptation of the Visual Basic code from pages 15 to 17 of [26] to Matlab (see Matlab Code for Summations, 66). It can be seen that the plots are virtually identical to those of the benchmark in Figure 4.8.

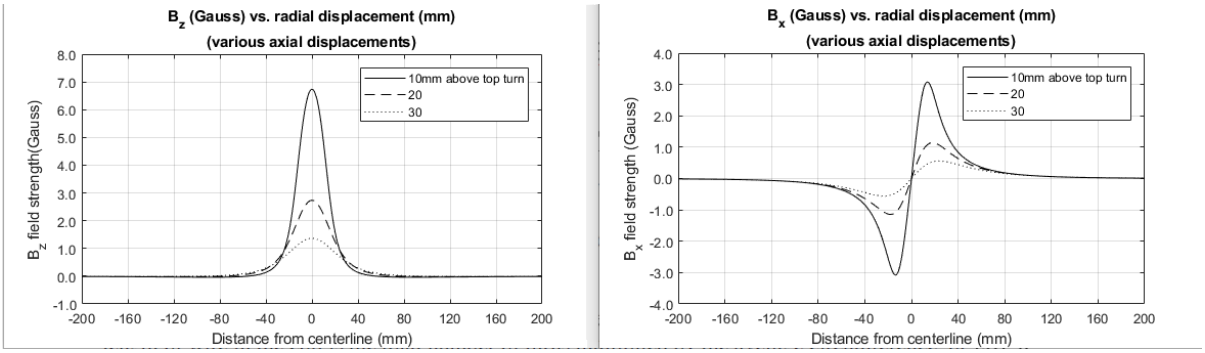

Figure 4.9: Matlab plot of Summation equations for magnetic field

Shown next is the benchmark using elliptic integrals to demonstrate their plotted results similarity.

4.1.7 Elliptic Integral Proofing

The following figure shows the plots obtained from adaptation of the Visual Basic code using the elliptic integrals and basic outline from pages 15 to 17 of [26] to Matlab (see Matlab Code for Elliptic, 69). Also, here, the plots are virtually identical to those from the benchmark example.

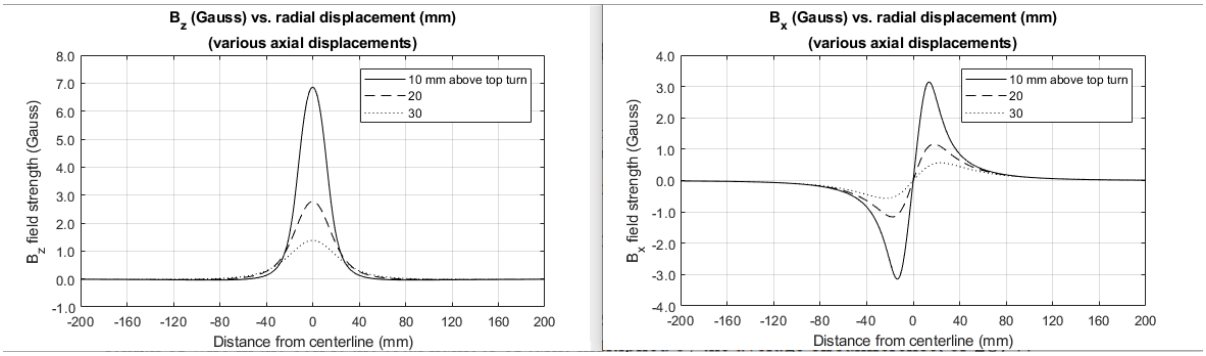

Figure 4.10: Matlab plot of Elliptic integral equations for magnetic field

A summary of comparative ***B*** field component nomenclature follows.

4.1.8 Summary

Although both of the above Matlab plot pairs show excellent results patterned as in the plots of the example of subsection 4.1.5, it is notable that the summation scheme here generates results in about nine and a half minutes, while on the same computer system, the elliptic scheme generates a virtually identical result in about one second. Thus the elliptic was the chosen result to move forward and process with.

The following table summarizes the expressions used for the components of **B** in the previously presented subsections of 4.1.1 through 4.1.4 as well as the representations of the components of **B**, moving forward, as general, given with respect to the coil top. The representations for the off-axis method are listed as spherical (B_r and B_θ) while the remaining are Cartesian.

Table 4.1: B field component summary

	On Axis	**Off Axis**	**Elliptic**	**Summation**	**General**
Vertical	$\bar{B}$	*Spherical*	B_x	B_z	B_z
Horizontal	*N/A, on axis*	*Spherical*	B_r	B_x	B_x

FEA software applied to the benchmark example is provided next.

4.1.9 FEA Analysis, Air Core

The benchmark coil of subsection 4.1.5 was modelled in COMSOL Multi-Physics FEA software using a parametric sweep and produced the results presented in Figure 4.11. The COMSOL results were in discrepancy with those from the Matlab coding, but of the same order of magnitude. This multiplier is not consistent for the entire sweep, possibly following a normal or Euler-form distribution depending on position relative to the coil geometry, the determination of which is left to future work.

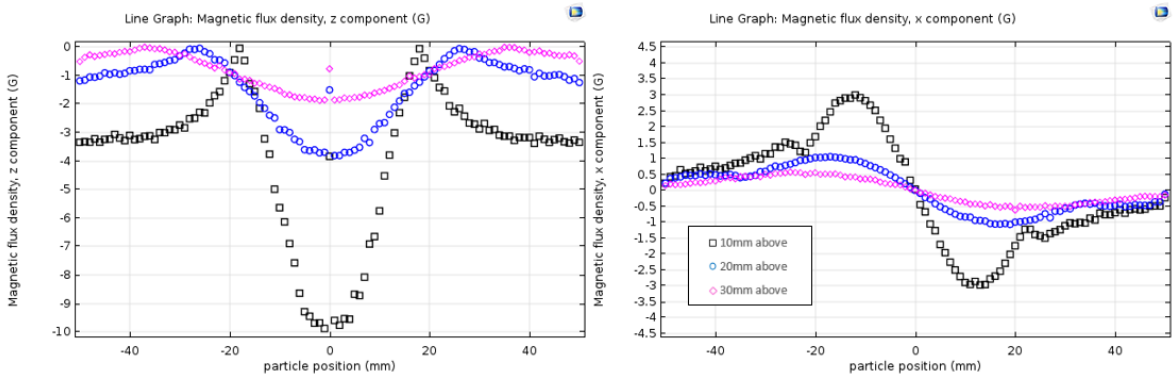

Figure 4.11: COMSOL B field components plot for benchmark coil

Due to the complexities involved, the FEA results were assumed to govern. Presented next are issues surrounding introduction of an iron core to the benchmark to increase magnetic field strength.

4.2 Introduction of Iron Core Issues

Applications herein did not involve a focus on the coil central body as an actuator such as in an automotive starter solenoid, but on the special application where the magnetic field produced and maintained at the coil ends affects the path of an iron particle while under its influence. At this stage of the research, an iron core was introduced as a field intensifier.

When the iron particle is brought into relative proximity to the coil, magnetization, **M**, enters the equations for force calculations. With **B** and **M** in the equations, further discrepancy as introduced in subsection 4.1.9 becomes evident in magnitude for the electromagnetic force components. It is compounded by the magnetization from the introduction of the iron particle and an iron core presence, with an expected distributed multiplier similar to the description in subsection 4.1.9.

Determination of an iron core factor was suggested and its determination was attempted, however this factor was determined not to be a constant, but also to have variability with regard to position of the particle, relative to the coil geometry. Attempts to construct an iron core factor matrix using data from FEA analyses led to the determination that future work is again required here. The FEA results were once again taken to govern.

Presented next is considerations regarding number of dimensions (2D, 3D) required for the continuance of FEA modeling when an iron particle is present in the magnetic field.

4.2.1 Choice of FEA Analysis Method

For the analysis with an iron particle present, it was established that an axisymmetric modelling method was inappropriate as dictated by the particle presence and the fact that in this environment it would improperly be revolved as a torus. A three dimensional modelling method was chosen. Particle tracing was not used as the iron particle charge was neutral. Further, required moving mesh constraints made the use of the Fluid-Particle Interaction module of COMSOL Multi-Physics inappropriate. For the magnetic field and electromagnetic force determinations, the COMSOL modelling method chosen relied solely on use of the AC/DC module for Magnetic Fields.

The next sections focus is on model results.

4.3 Model Results

The established regimen of programming in Matlab and modelling in COMSOL, from this chapter, is carried out in this section with further comparison using the benchmark of subsection 4.1.5.

A small ferromagnetic spherical particle of soft iron is treated as an induced magnetic dipole from its presence in the magnetic field. The applied equations of force, magnetic field, and magnetic field gradient are introduced with results displayed from graphical output of the software in the opening pages of Chapter 5.

Presented first, here, is electromagnetic force consideration.

4.3.1 Force

The following equations, (4.16) and (4.17), developed within [28] are used to display and evaluate the force on a magnetized object from a magnetic field as first described in section 3.4.

$$\boldsymbol{F} = \int_V (\boldsymbol{M} \cdot \boldsymbol{\nabla}) \boldsymbol{B}_{ext} dv \;\; (where \; \boldsymbol{\nabla} \times \boldsymbol{B} \; and \; \boldsymbol{\nabla} \cdot \boldsymbol{B} \; are \; both \; zero \; in \; its \; development) \qquad (4.16)$$

Within (4.16) the following equation (4.17) in terms of magnetization components and magnetic field gradients is defined.

$$\begin{aligned} (\boldsymbol{M} \cdot \boldsymbol{\nabla}) \boldsymbol{B}_{ext} = & \left(M_x \frac{\partial}{\partial x} + M_y \frac{\partial}{\partial y} + M_z \frac{\partial}{\partial z} \right) B_{ext_x} \hat{x} \\ & + \left(M_x \frac{\partial}{\partial x} + M_y \frac{\partial}{\partial y} + M_z \frac{\partial}{\partial z} \right) B_{ext_y} \hat{y} \\ & + \left(M_x \frac{\partial}{\partial x} + M_y \frac{\partial}{\partial y} + M_z \frac{\partial}{\partial z} \right) B_{ext_z} \hat{z} \end{aligned} \qquad (4.17)$$

NOTE: Due to complexities involved with determining magnetization components for a ferromagnetic particle analytically, reliance was placed on the FEA software to provide the components of force.

Expressions for the magnetic field components are shown previously, but their gradients are not. The following subsection reviews the field components using a different set of variables, also used in Appendix E to describe the nine gradient expressions within (4.17).

4.3.2 Magnetic Fields

Equations (4.18) to (4.22) and Figure 4.12 presented from [27], for further use in Appendix E, describe the magnetic field with respect to a circular current loop. Superposition was used in their application to approximate the field from an air core solenoid in Matlab. They make use of complete elliptic integrals of the first and second kind.

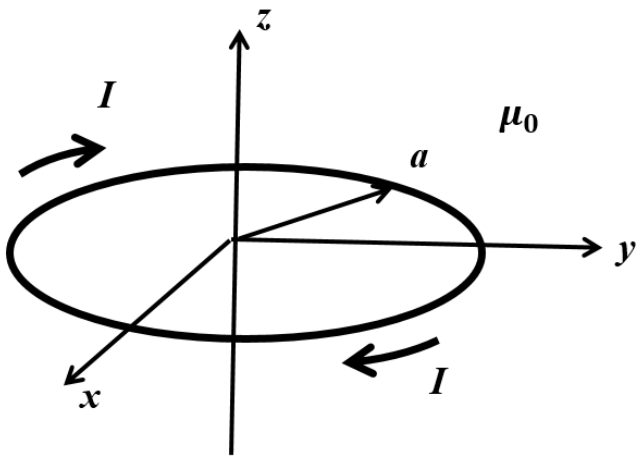

Figure 4.12: Circular current loop geometry, [27].

The following substitutions are made for simplicity:

$$\rho^2 \equiv x^2 + y^2, r^2 \equiv x^2 + y^2 + z^2, \alpha^2 \equiv a^2 + r^2 - 2a\rho, \beta^2 \equiv a^2 + r^2 + 2a\rho, k^2 \equiv 1 - \frac{\alpha^2}{\beta^2} \qquad (4.18)$$

$$\gamma \equiv x^2 - y^2, C \equiv \mu_0 \frac{I}{\pi}, from\ which\ \rho \geq 0, r \geq 0. \qquad (4.19)$$

In the above, I represents current, and μ_0 is the permeability of free space.

The magnetic field components are:

$$B_x = \frac{Cxz}{2\alpha^2\beta\rho^2}[(a^2 + r^2)E(k^2) - \alpha^2 K(k^2)] \tag{4.20}$$

$$B_y = \frac{Cyz}{2\alpha^2\beta\rho^2}[(a^2 + r^2)E(k^2) - \alpha^2 K(k^2)] = \frac{y}{x}B_x \tag{4.21}$$

$$B_z = \frac{C}{2\alpha^2\beta}[(a^2 - r^2)E(k^2) + \alpha^2 K(k^2)] \tag{4.22}$$

In the above, $K(k^2)$ is the complete elliptic integral function, of the first kind, and $E(k^2)$ is the complete elliptic integral function, of the second kind.

From this, the magnetic field gradients can be shown with similar variable definition. They are presented in Appendix E.

Use of the preceding information allows additional analysis when an iron particle is introduced to the magnetic field environment and this is presented next in the opening pages of Chapter 5, as a lead-in to simulations.

Chapter 5
Finite Element Model

In this chapter, the equations of section 4.3 are used in calculations in Matlab through programming for the multi-turn, multi-layer air core solenoid of the example benchmark of subsection 4.1.5, first. Then the same solenoid is modelled in COMSOL for comparison. Analyzing this same solenoid in Matlab, but with an iron core proved difficult due to the iron core presence. It is studied here with the use of the FEA software, COMSOL Multi-Physics, and not analytically in Matlab. The analytical process clarifications are left to future work as outlined in Chapter 7.

The soft iron particle diameter used at this stage for analytical and comparative simplicity was one millimeter (1000 microns). Later stages for experimental purposes reduce this size to the aforementioned particle spherical diameter of 125 microns. The electromagnetic forces involved are applied for the first time, here.

Further presented are the results of developing an optimal coil configuration by coil parameter adjustments and amperage increase with real world wire gauge selection for current carrying compliance. Then a permanent magnet configuration was developed to produce an approximately similar magnetic field strength presence compared to that of the optimum coil. Magnetic field and electromagnetic force magnitudes for comparisons are presented in Table 5.2. Lastly, post-processing in Matlab to achieve the particle path diversion plots is presented. This serves to confirm that the soft iron particle modelled in the system would in fact undergo a simulated change in direction under the influence of the magnetic field presence.

5.1 Air Core

The equations of section 4.3 were used with the code in Matlab (see Matlab Code for Force, 71) to produce the electromagnetic force plot of Figure 5.1: Matlab electromagnetic force component plots for benchmark.

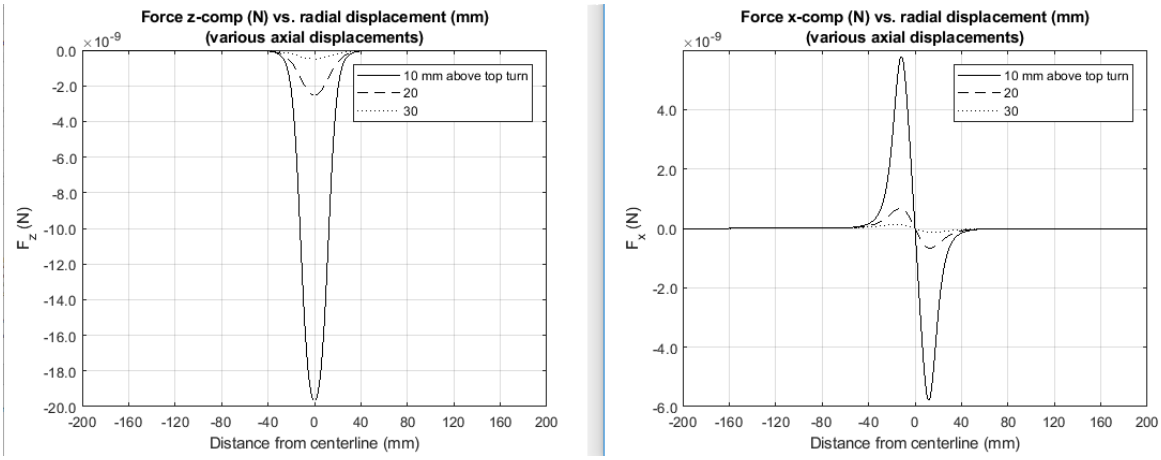

Figure 5.1: Matlab electromagnetic force component plots for benchmark

The same coil modelled in COMSOL using FEA produced similar shaped plots within approximately twenty percent. Further study of the anomalies here is left to future work. Figure 5.2: COMSOL plots of the electromagnetic force for benchmark example, is provided, below, for comparison to Figure 5.1.

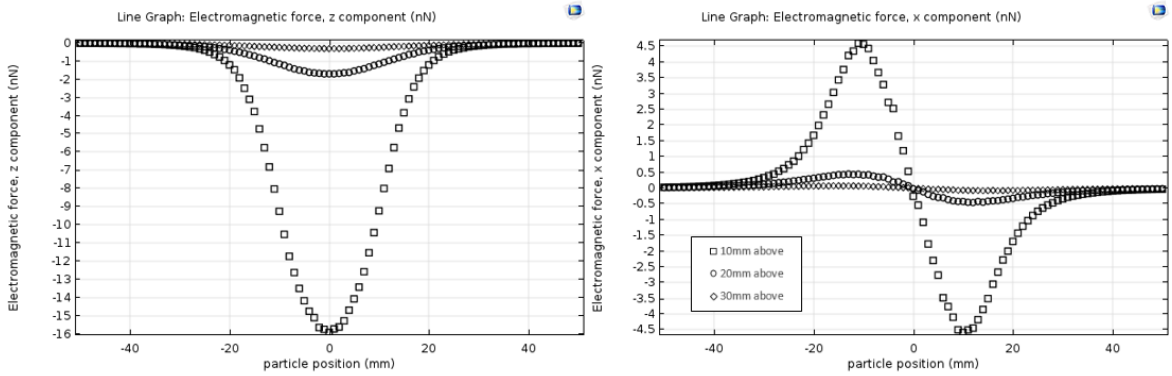

Figure 5.2: COMSOL plots of the electromagnetic force for benchmark example

From this we can see that the general shape of the plots is very similar when the different scales of the plot axes of Figure 5.1 and Figure 5.2 are considered. The discrepancy does appear to have some correlation in the plot results to that first described in subsection 4.1.9, again, future work. Here, again the FEA results were taken to govern.

The next section involves adding an iron core to the simulation to provide a magnetic field strengthening in order to increase the electromagnetic force available to act on an iron particle.

5.2 Iron Core

The addition of a soft iron core acted to definitively increase the magnetic field component magnitudes and the electromagnetic force component magnitudes. The FEA plots for the benchmark example are provided in Figure 5.3 and Figure 5.4 for both.

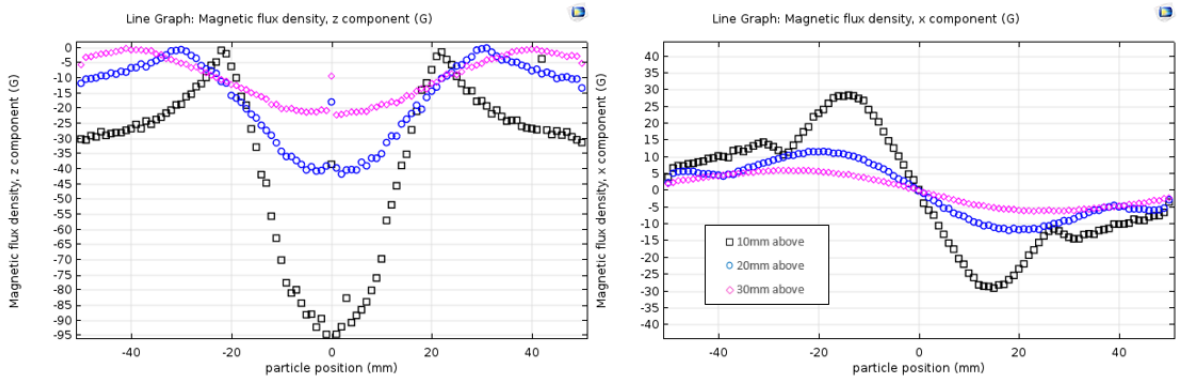

Figure 5.3: Magnetic field component plots of benchmark example with addition of iron core

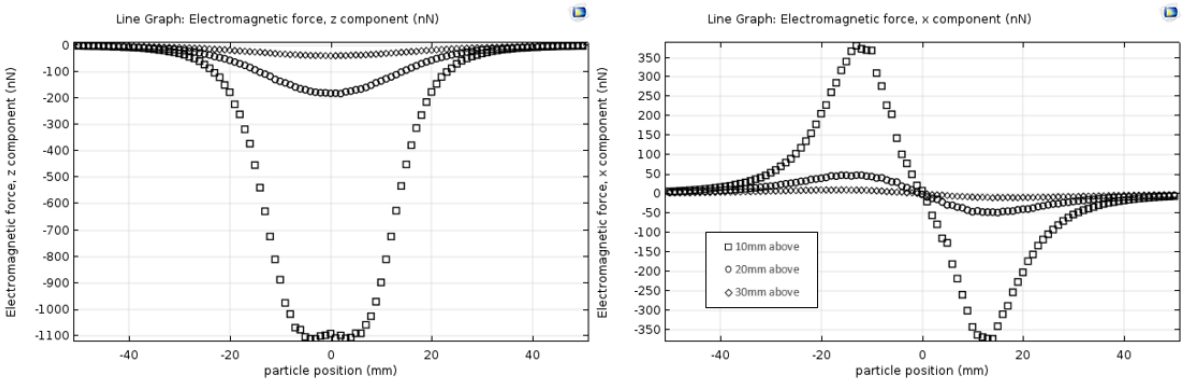

Figure 5.4: Electromagnetic force component plots of benchmark example with addition of iron core

From this we can see the plausibility of adding an iron core and the general effects on the magnetic field and electromagnetic force components generated evident from the change in force axis range from the tens of nano-Newton of Figure 5.2 to the thousand nano-Newton range of Figure 5.4, an approximate 100 fold increase.

Next, the coil parameters such as configuration of number of turns and number of layers of wire, wire gauge, and current are tuned in order to produce a coil construct capable of providing sufficient force to attempt particle diversion studies.

5.2.1 Coil

With the addition of an iron core, force strength magnitudes reached into the micro-Newton range from the previous nano-Newton range of the air core solenoid originally introduced. From here it was appropriate to develop coil parameters for configuration optimization. Programming in Matlab was used to select parameters in order to produce a maximum applied electromagnetic force to a typical iron particle. The particle used was spherical, and one millimeter in diameter here. The magnetic field and electromagnetic force plots for the best coil are provided in Figure 5.5 and Figure 5.6. They show forces now developed in the milli-Newton range.

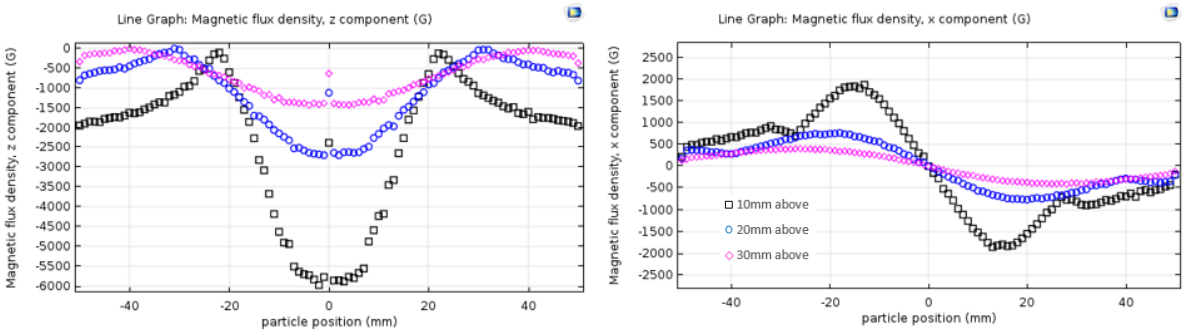

Figure 5.5: Plots of magnetic field components for best coil

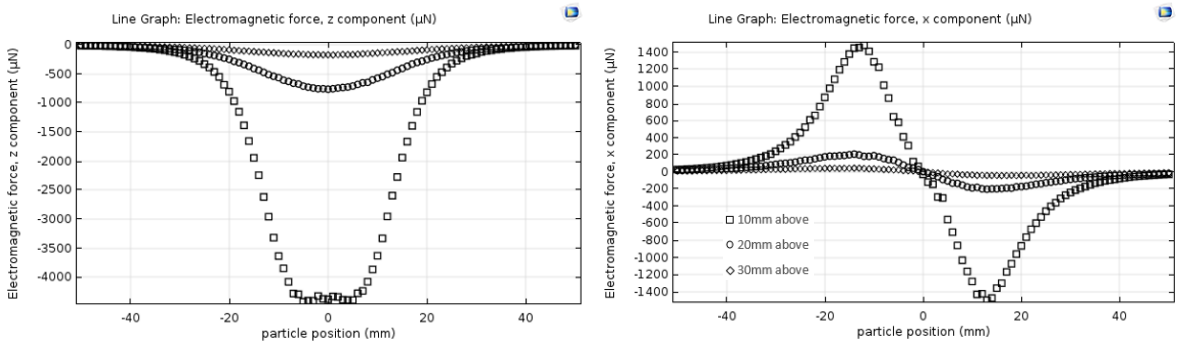

Figure 5.6: Plots of electromagnetic force components for best coil

The best coil parameters are given in Table 5.1. It is noted that the wire gauge chosen allowed a current boost to 5A, approximately 80.1 times more current than that of the benchmark example of 4.1.5. It is further notable that current is a constant linear multiplier to the **B** field components as shown in the equations throughout Chapter 4.

Table 5.1: Best coil parameters

Current	**Wire gauge/ sheathed diameter**	**Turns**	**Layers**	**Inner radius (core)**
5A	*22AWG/0.714mm*	*148*	*31*	*10mm*

With this configuration establishing a usable upper bound on field and force, it was necessary to switch constructs from a coil configuration to a permanent magnet configuration. This enabled development of a practical experimental apparatus that could be used in a laboratory setting with available equipment.

The use of permanent magnets is introduced next.

5.2.2 Permanent Magnets

Permanent magnets can be used to substitute for an electromagnetic coil to produce a magnetic field of similar shape to that of the coil. In order to develop forces of the magnitude of the best coil of subsection 5.2.1 it was necessary to obtain neodymium permanent magnets of maximum strength rated as N52. Those obtained had surface fields on the order of 6450 Gauss for a one inch cube form magnet, for example.

Several magnet configurations were considered and it was decided a one inch cube would be used for magnitude of force development. Additionally, a ten millimeter diameter by four millimeter height permanent magnet, central on top of the cube, as shown in Figure 5.7, was added. This would act to locally focus the magnetic field above the construct. A one millimeter diameter iron particle is shown in close proximity in the figure.

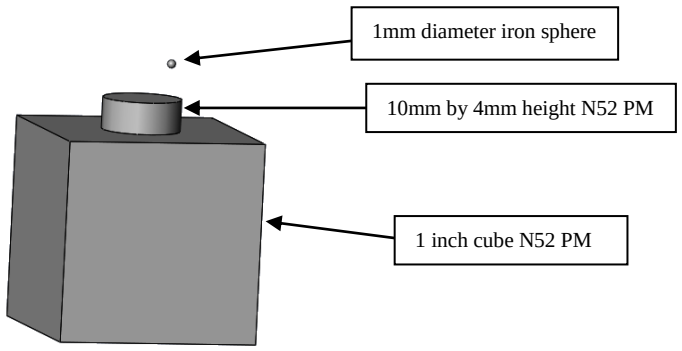

Figure 5.7: Initial one inch cube PM configuration

Magnetic field and electromagnetic force plots from the FEA software for the Figure 5.7 permanent magnet (PM) configuration are provided in Figure 5.8 and Figure 5.9. A remanence of 1e6 A/m was used for the FEA simulations.

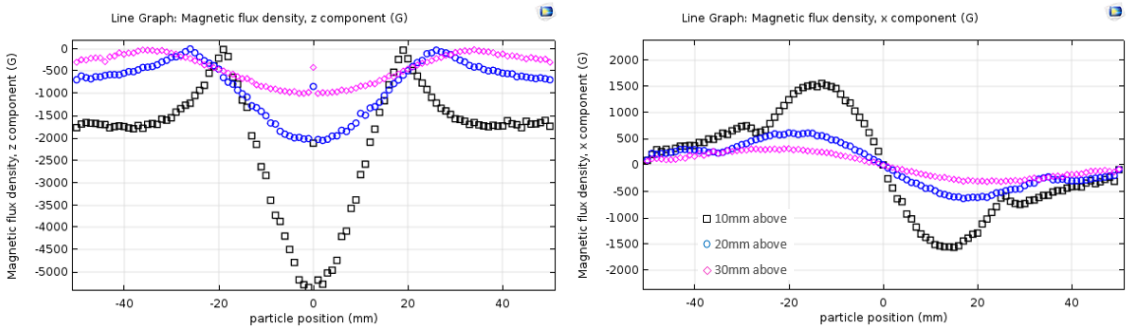

Figure 5.8: Plots of magnetic field components of initial PM configuration

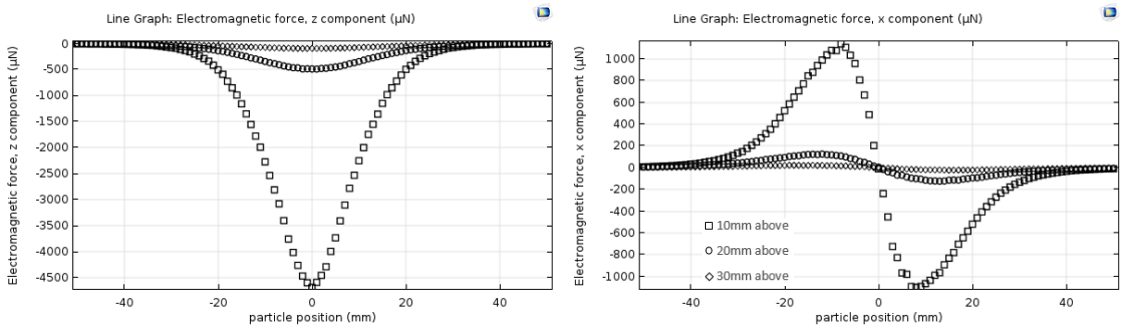

Figure 5.9: Plots of electromagnetic force components of initial PM configuration

The above curves are not identical to Figure 5.5 and Figure 5.6. However, their shape is very similar, with magnitude size similar and approximately equal maximums achieved. For this reason, these were assumed a comparatively suitable substitute to the best coil with iron core of 5.2.1.

Next, comparative results are presented for maximums achieved for magnetic field and electromagnetic force components of this chapter's considerations.

5.3 Obtained Results Summary

Table 5.2 summarizes the magnetic field component and electromagnetic force component maximums obtained for the results of Chapter 5, and related portions of Chapter 4. The air core results from Matlab to COMSOL show the approximate twenty percent discrepancy as outlined in

subsection 4.1.9 (FEA taken to govern). Adding the iron core provides the definitive boost described in section 5.2. Varying the coil parameters to obtain the best result (see Table 5.1), with a current boost from 62.4mA to 5A, allowed the results of subsection 5.2.1. Further, the coil results had their approximate magnitude achieved using a permanent magnet configuration from subsection 5.2.2.

From here, the focus was on the use of a permanent magnet construct in place of the best coil construct.

Table 5.2: mf and emf component maximums at 10mm above coil/PM

	Air core, Matlab	**Air core, COMSOL**	**Iron core, COMSOL**	**Coil, COMSOL**	**1" PM, COMSOL**
Section/Subsection	**4.1.5**	**4.1.9**	**5.2**	**5.2.1**	**5.2.2**
$\mathbf{B_x}$	*3G*	*3G*	*30G*	*1900G*	*1500G*
$\mathbf{B_z}$	*7G*	*10G*	*95G*	*6000G*	*5500G*
$\mathbf{F_x}$	*6nN*	*4.5nN*	*375nN*	*1500μN*	*1200μN*
$\mathbf{F_z}$	*20nN*	*16nN*	*1100nN*	*4500μN*	*4700μN*

The next section introduces FEA results post-processing in Matlab to allow determination of particle trajectory, or particle path diversion, using parametric sweeps in COMSOL Multi-Physics.

5.4 Post-Processing in Matlab

In order to develop ferromagnetic particle positional information, results from parametric sweeps in COMSOL were copied and structured in MS Excel. These were read into Matlab and saved as .mat files for further use as double interpolation lookup tables. These tables were then used as force data to solve the ode45 differential equation set (see Matlab Code and Function for Trajectory, 75). From this the plots of Figure 5.10 and others like them were developed. Here, the initial particle speed was 5 m/s, downward and this was later changed to 2 m/s, as in the literature, [37]. Initial position was 20mm above the PM, with x-position as noted in the figures as variable.

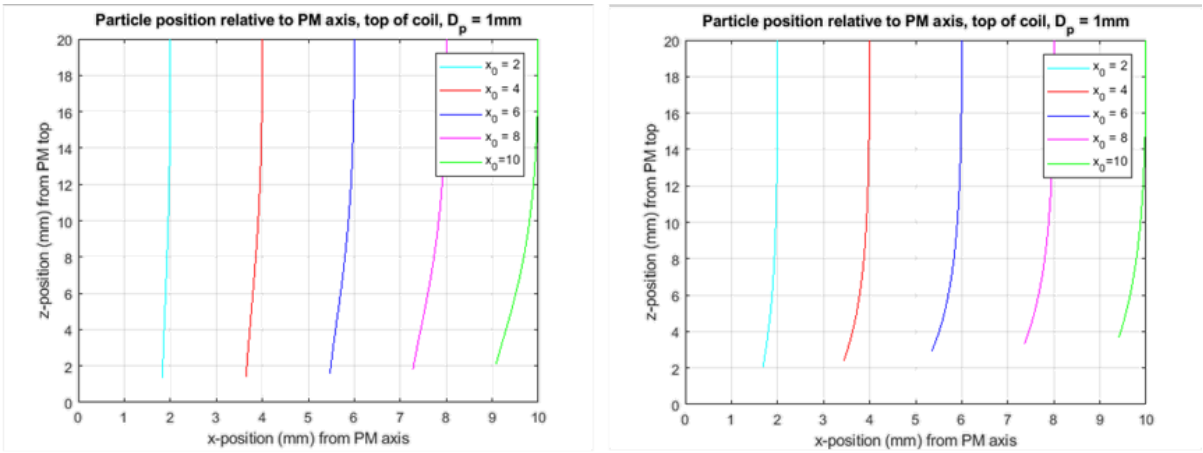

Figure 5.10: One inch cube configuration particle trajectories

The results plotted in Figure 5.10 show trajectories for the one inch cube (left) and one inch cube with ten millimeter diameter, four millimeter (10/4) height cylindrical addition (right) N52 permanent magnet of Figure 5.7. The top of the magnet was set as zero elevation and the central core axis of each magnet construct was at x-position zero. From this, it is seen that there is definite variability in the particle trajectories from the left half of Figure 5.10, and the right. There is increased horizontal draw in the two to six millimeter x_0 paths (left half of figure to right) and there is decreased horizontal draw for eight and ten. This serves to prove greater focus to be achievable closer to a melt pool with the use of the 10/4 addition.

From here, it was determined that the magnet configuration be studied with efforts directed at improving the intensity of the inward draw close to the central magnet configuration axis. Addressing this proximity interest with regard to a typical additive manufacturing melt pool build zone was deemed to be most appropriate. Findings regarding this study are the principle focus in the following.

Chapter 6
Refinement of Permanent Magnet Configurations

With the confirmation of trajectory modification of section 5.4, further study into optimizing the permanent magnet configuration was undertaken and is described here. Several configurations were analyzed, based first on shape of the main body, then on permanent magnets on-hand. The post-processing method of section 5.4 was used to obtain the plots discussed in section 6.3 for select configurations only. The remainder have results mentioned (not presented) from COMSOL modelling.

Here, a 125 micron maximum diameter spherical particle was used in place of the 1000 micron to be more representative of actual AM particle diameters. With this reduced size, the initial particle speed of 5 m/s, downward was changed in magnitude to 2 m/s, as in the literature [37]. Initial position was considered to have z-coordinate 20mm above the PM, with x-coordinate set similar to that used to develop the results of section 5.4 with reference to the central axis of the PM construct as zero.

A summary of the configurations which were modeled is presented next.

6.1 Summary of Configurations Modelled

Parametric sweeps of the configurations here were used to generate force component plots in x and z. Four sets of figure series were generated based on PM main body shape including:

1. 13 mm by 13 mm cylindrical
    a. Base shape (1 shape)
    b. Base shape with 10 mm diameter by 4 mm height cylinder atop (1 shape)
2. 19.05 mm, and 25.4 mm cubic (2 separate cubic shapes)
3. 38.1 mm, and 50.8 mm spherical (2 separate spherical shapes), and
4. 19.05 mm, and 25.4 mm cylindrical (2 separate cylindrical shapes).

Each main body shape was simulated as follows, each for three particle diameters of 0.125, 0.5, and 1mm:

1. Main body alone
2. Main body with 2mm by 4mm PM atop
3. Main body with 2mm by 8mm PM atop

These 72 simulations were documented and referenced to determine choice of configurations to emulate from available permanent magnets on hand, presented in the next section.

6.2 Readily Available Configurations Modelled

The set of figures that follow Table 6.1 (Figure 6.1 to Figure 6.5) show the electromagnetic force components on a resident iron particle of 0.125mm diameter obtained using a parametric sweep in COMSOL Multi-Physics. The particle position is shown relative to the central axis of a permanent magnet (PM) configuration and plots are given for three different elevations (2, 5, and 10 mm) above the topmost part of the magnets. Summarized force data for three different particle diameters (0.125, 0.5, and 1 mm) is given in Table 6.1 for each configuration. Only 0.125mm particle diameter plots are given, for relevant brevity.

The five configurations presented include:

1. A 10mm diameter by 10mm height PM with a 2mm diameter by 4mm height PM atop
2. A 10mm diameter pair of PM stacked, with a 2mm diameter by 4mm height PM atop
3. A 25.4mm diameter PM, of 19.05mm height, with a 2mm diameter by 4mm height PM atop
4. A 10mm diameter by 10mm height PM with a 4mm diameter by 1.5mm height PM atop, and
5. A 25.4mm diameter PM, of 19.05mm height, with a 4mm diameter by 1.5mm height PM atop

Table 6.1 summarizes the maximum force magnitudes for each configuration and particle size studied here.

Table 6.1: Maximum force magnitudes for five configurations and three particle sizes

Spherical particle diameter (mm)	**Configuration**	**Fx max (µN)**	**Fz max (µN)**
0.125	*1*	*10*	*40*
	2	*10*	*40*
	3	*18*	*75*
	4	*30*	*112*
	5	*45*	*130*
0.5	*1*	*600*	*2300*
	2	*620*	*2600*
	3	*1200*	*4700*
	4	*1900*	*7100*
	5	*2500*	*8500*
1	*1*	*4500*	*19000*
	2	*5000*	*21000*
	3	*9200*	*38000*
	4	*16000*	*57500*
	5	*20000*	*62500*

Note: Configuration 2 had none to marginal increase in force component maximums compared to configuration 1 and was thus disregarded in further study. The remaining were carried forward, as presented next.

Figure 6.1 to Figure 6.5 show the electromagnetic force components a resident iron particle of 0.125mm diameter experiences when in relative proximity to the given PM constructs. The plots were obtained using a parametric sweep in COMSOL Multi-Physics. The particle position is shown

relative to the central axis of a given permanent magnet (PM) configuration and plots are given for three different elevations (2, 5, and 10 mm) above the topmost part of the magnets.

Two of the configurations are presented as proposed for future experiments in Future Work and Recommendations, section 7.2 (item v.).

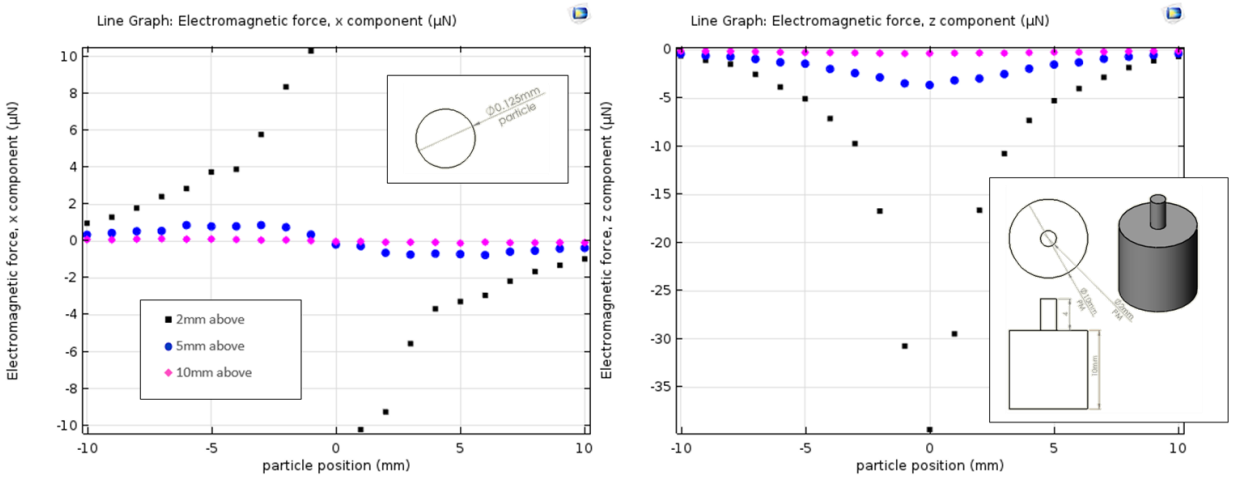

Figure 6.1: 10mm PM with 2mm by 4mm PM, configuration 1

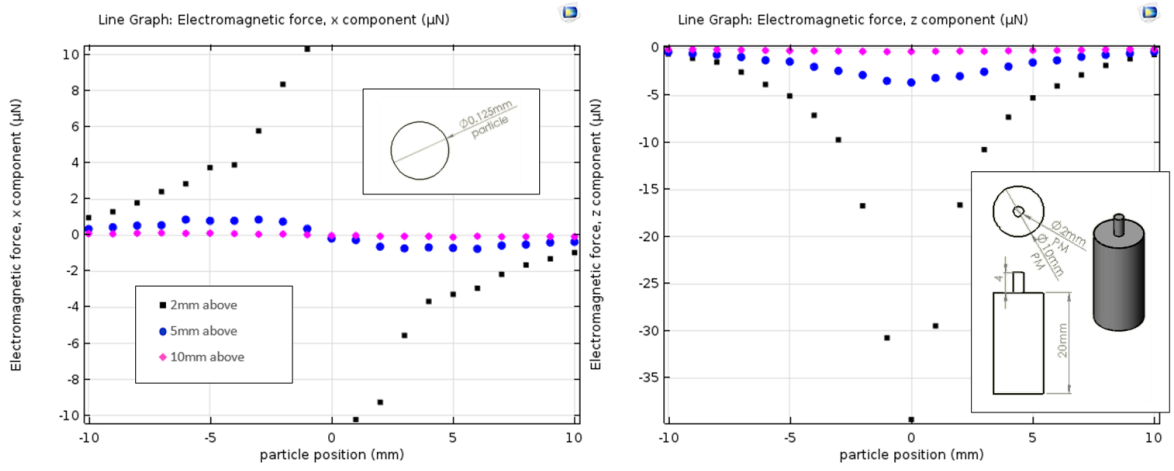

Figure 6.2: 10mm PM stacked, with 2mm by 4mm PM, configuration 2

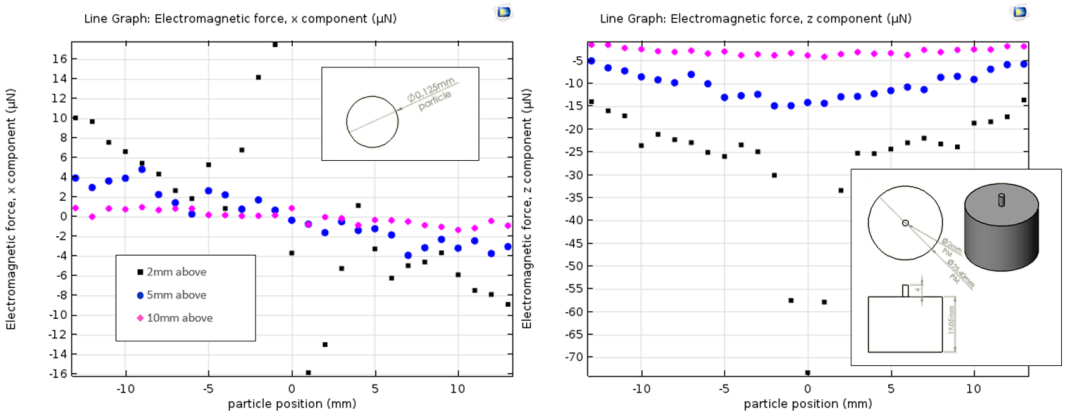

Figure 6.3: 25.4mm PM, 19.05mm height, with 2mm by 4mm PM, configuration 3

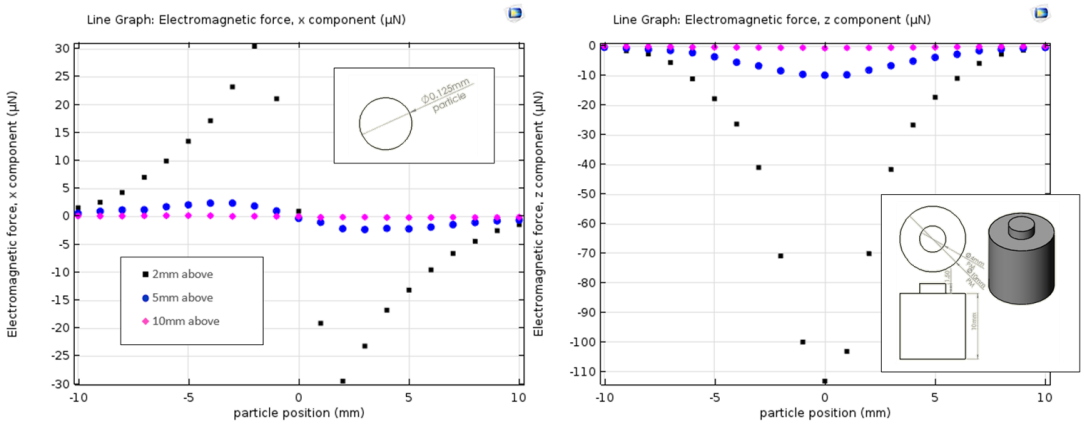

Figure 6.4: 10mm diameter by 10mm height PM with a 4mm diameter by 1.5mm height PM atop, configuration 4

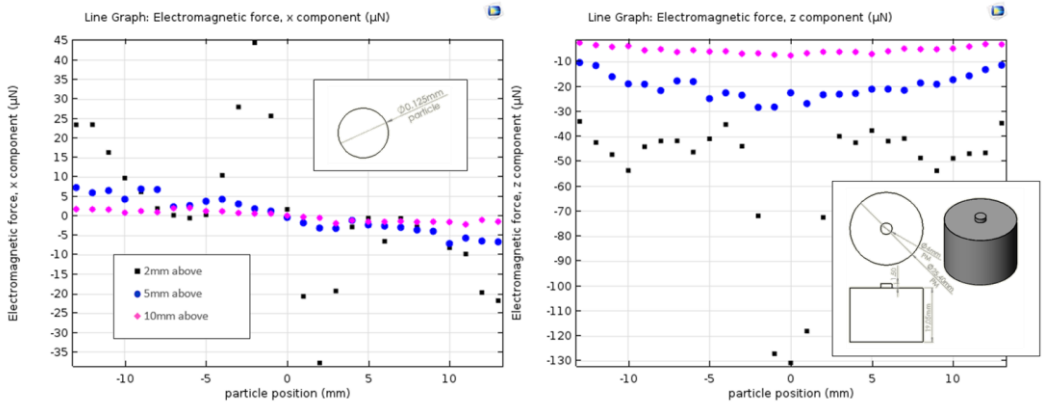

Figure 6.5: 25.4mm diameter PM, of 19.05mm height, with a 4mm diameter by 1.5mm height PM atop, configuration 5

It is evident from the above figures that the force component magnitudes are in the micro-Newton range. It is also shown that the greatest magnitudes are experienced in the region close to the AM build zone, as desired.

The following section describes the particle trajectories for four of the five above PM configurations.

6.3 Selected Configuration Trajectories

Configurations 1, 3, 4, and 5 from section 6.2 next had force lookup tables, first noted in section 5.4, constructed for a complete set of elevations from 1 to 20 mm above the magnets. COMSOL modeling was used with a parametric sweep, to generate force data for use in Matlab. In Matlab, the ode45 differential equation method was used to determine particle path plots while under the force lookup networks. Table 6.2 shows the magnet configuration parameters using dimensions according to the key, Figure 6.6.

For these, the 0.125mm diameter spherical iron particle was given initial x-coordinate position of 1, 2, to 10 mm displacement in the x-direction from each permanent magnet configuration central, vertical axis. A height of 20mm above was used for the initial z-position. An initial velocity of 2 m/s vertically downward was also used.

It is notable that the previously used initial velocity of 5 m/s downward was discarded here, as no discernible lateral deflection was evident in the plots when it was used. Also, the 2 m/s is approximately in agreement with [37] where velocity of the particle is equal to the gas mass flow rate divided by the powder delivery interior nozzle area.

The contents of Table 6.2 represent the bulk of the configurations which could relatively be constructed from PM's that were readily available.

Table 6.2: PM configuration parameters

Section 6.2 PM Configuration	Section 6.3 PM Configuration	a (mm)	b (mm)	c (mm)	d (mm)
1	1	10	10	2	4
4	2	10	10	4	1.5
3	3	25.4	19.05	2	4
5	4	25.4	19.05	4	1.5

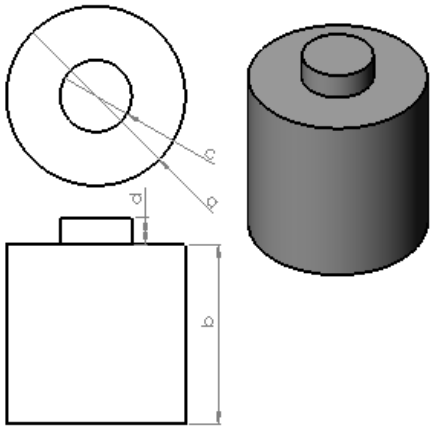

Figure 6.6: Permanent magnet configuration dimensions key

The plots for these configurations are provided in Table 6.3. Here, configuration 1 showed little deviation from the vertical until at the elevation of the substrate which configuration 2 markedly improved. Configuration 3 showed similar draw, but breaks from the vertical much sooner and configuration 4 improved on this.

It is notable that the concept of introducing these configurations was to produce a localized greater draw in the vicinity of the typical melt pool location. All but configuration 1 readily showed this to be evident as seen by the break of the x_0 = 1 mm to x_0 = 3 mm range. From this it is indicated that configuration 2 and either 3, or 4 would represent likely candidates for experimental verifications (reference item v. of section 7.2).

Table 6.3: Particle paths of proposed configurations

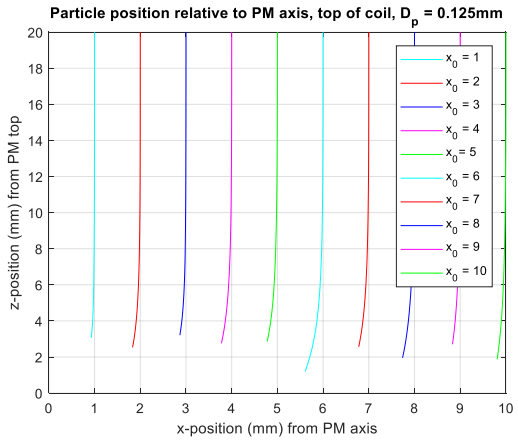

Figure 6.7: Configuration 1 particle paths

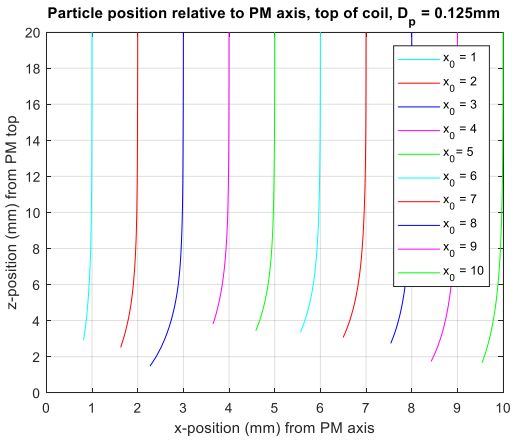

Figure 6.8: Configuration 2 particle paths

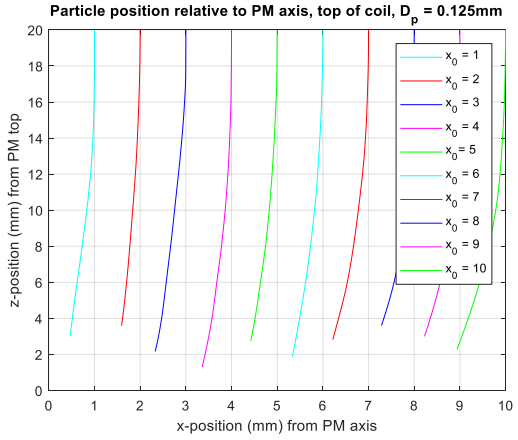

Figure 6.9: Configuration 3 particle paths

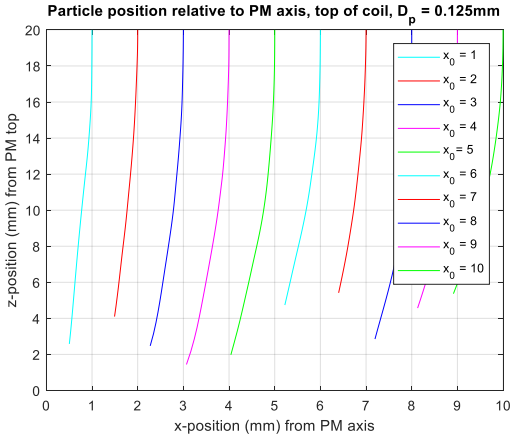

Figure 6.10: Configuration 4 particle paths

Proposed Experimental Studies are mentioned next.

6.4 Proposed Experimental Studies

Appendix F (with initial details in section 7.2) presents some details regarding proposed experimental studies. A proof of concept method for initial study and two main experimental procedures are suggested. Also, a figure detailing suggested apparatus is provided.

Conclusions and Future Work are presented next.

Chapter 7
Conclusions and Future Work

7.1 Conclusions

In this thesis, introduction of a novel but constructive approach to implement catchment efficiency improvement with regard to ferromagnetic particle path diversion was addressed. The potential to increase their density in proximity to the melt pool region through introduction of a magnetic field from either a permanent magnet, or electromagnetically with a coil, was used. It was shown through simulations that this field would act to produce a lensing or concentric constriction focus of the particle stream above as its contents near and enter the AM build zone.

Of the four analytical methods to determine the magnetic (**B**) field either on or off the axis of a solenoid studied, the two chosen (summation, and elliptic integral) verified Matlab programming from an established benchmark example. The FEA model constructed to provide simulations using a soft iron particle to determine validity of Matlab programming showed a discrepancy in the **B** field and further discrepancy for the electromagnetic force, over Matlab, for the air core solenoid benchmark. This led to analysis dependent on FEA software only, moving forward. Introduction of permanent magnet configurations in place of a coil was decided to simplify constructs for future proposed experimental considerations.

Parametric sweeps in the FEA software for given coil and permanent magnet configurations generated force data for post-processing in Matlab. This was used to produce particle displacement plots using differential equations. Successful determination of particle path diversion was confirmed for the four selected permanent magnet configurations, chosen from available magnets in stock to provide constructs with which to move forward with experimentally.

7.2 Future Work and Recommendations

Although the analysis and simulations presented in this thesis show a definite change in a soft iron particle path while under the influence of a given magnetic field, there are several considerations or improvements with the following recommendations regarding future work to be considered:

i. The contents of the melt pool for ferromagnetic material can have its shape altered by the introduction of a magnetic field to the AM build zone. Future work may involve analysis and evaluation of such melt pool geometry considerations through substantiation of their effects.

ii. Another inadequacy encountered involved introduction of the iron core to the air core solenoid and the magnitude or distribution of what could be termed as the iron core factor. It is proposed that experiments, possibly leading to publishing, be undertaken to potentially determine a mathematical method to define an equation for this factor based on position relative to coil geometry.

iii. A method to apply the process studied to an actual AM build using generally accepted processes, inclusive of angling the powder stream and using active lasers, and having a controlled construct for the magnetic field (possibly a coil with electric current adjustable) is suggested. This would serve to provide a more complete validation of the intended effects.

iv. Determining a way to control the magnetic field component magnitudes by use of an electromagnetic source in place of permanent magnet constructs in order to allow the particles additional time in the effective field, under greater inward draw, could serve to improve the process. The iron particles would then be directed further inwards to the central lasing region, as intended within. Additionally, using an electromagnet with a variable magnetic field would allow for height compensation during a build process.

v. Conducting the proposed proof of concept presented in Appendix F, and experiments, is a logical, and foreseen aspect for future work. This would provide confirmation of the underlying concepts and simulations presented in this thesis. The simulation process does serve to preliminarily confirm, with proposed additional experiments that would serve to validate.

Provided next is the experiment flow for proposed experiments.

7.2.1 Experiment Flow for Proposed Experiments

The intended experimental flow involves first establishing a powder type to use and its delivery process to the AM melt zone. An argon gas delivery system would establish this. Once substantially within reasonable proximity to the magnetic field source, it could be acted on via the magnetic field.

The next step would be to capture an image of the trajectory change compared to an image without the magnetic source present. From here, the before and after images could be processed in Matlab using an image command series of operations to verify a change in the particle stream intensity distribution as shown in Figure 2.1. Figure 7.1 shows the intended experiment flow process.

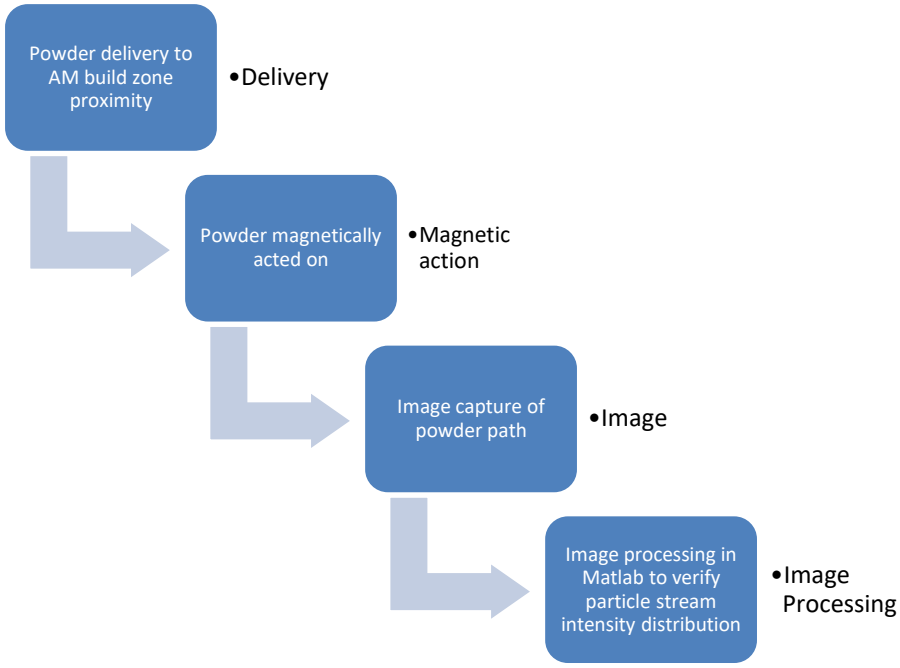

Figure 7.1: Experiment flow chart

Lastly, a brief description of two of the potential lab environment machines is presented.

7.2.2 Proposed Experiment Potential Lab Equipment

Two items of lab equipment that were to be used for conducting the experiments and any proof of concept efforts are as presented in Figure 7.2 and Figure 7.3. The powder delivery system is a Sulzer Metco Twin 10C powder feeder, and the CNC is a Fadal, model 88HS.

Both are capable of providing adequate functionality towards achieving the required outcome of having a powder delivered and a substrate translated beneath the powder stream. Permanent magnets to deflect the stream (in the vicinity of the stream) from beneath the substrate are readily available as described here in Chapter 6.

Photographic equipment suitable for the task of capturing the powder deflection event is yet to be determined. Also, appropriate lighting and backdrop are for future considerations.

Figure 7.2: Powder delivery apparatus

Figure 7.3: CNC equipment

References

[1] W. Syed, A. J. Pinkerton, et al, *Virtual modeling and rapid manufacturing: Statistical analysis of the effect of processing conditions on powder catchment efficiency in the Direct Laser Deposition (DLD) process*. London: Taylor & Francis Group, 2005, pp. 361-366. [Online]. Available: https://books.google.ca/books?id=muWKO0x1po8C&pg=PA361&lpg=PA361&dq=additive+manufacturing+catchment+efficiency&source=bl&ots=rzl8IN3r81&sig=d532kyrHSmJod108WGSLZyJ171g&hl=en&sa=X&ved=0ahUKEwia0-js3pXUAhWq6YMKHQv6BawQ6AEISjAH#v=onepage&q=additive%20manufacturing%20catchment%20efficiency&f=false. [Accessed: February, 2018].

[2] "Physics Stack Exchange," *physics.stackexchange.com*, October, 2014. [Online]. Available: https://physics.stackexchange.com/questions/143119/why-in-a-solenoid-do-the-magnetic-field-lines-resemble-that-of-a-bar-magnet and http://hyperphysics.phy-astr.gsu.edu/hbase/magnetic/elemag.html, (true source). [Accessed: February, 2018].

[3] A. Pinkerton, W. Syed, L. Li, "Theoretical analysis of the coincident wire-powder laser deposition process," ASME digital collection, J. Manuf. Sci. Eng., 129(6), pp. 1019-1027, 2007.

[4] C. Munro, N. Chambers, "Laser Additive Manufacturing of Monel K500: Effects of Pulsed Laser Parameters on Bead Shape," *cradpdf.drdc-rddc.gc.ca*, May, 2015. [Online]. Available: http://cradpdf.drdc-rddc.gc.ca/PDFS/unc203/p801819_A1b.pdf. [Accessed: February, 2018].

[5] C. Munro, H. Smiley, "Laser additive manufacturing of Monel K500: Processing map development," *cradpdf.drdc-rddc.gc.ca*, June, 2015. [Online]. Available: http://cradpdf.drdc-rddc.gc.ca/PDFS/unc194/p802297_A1b.pdf. [Accessed: February, 2018].

[6] Y. Lee, *Simulation of Laser Additive Manufacturing and its Applications*. PhD [Dissertation, Online]. Columbus, Ohio: Ohio State University, 2015. Available: https://etd.ohiolink.edu/!etd.send_file?accession=osu1440360229&disposition=inline.

[7] M. Alimardani, *Multi-Physics Analysis of Laser Solid Freeform Fabrication*. PhD [Thesis, Online]. Waterloo, Ontario: University of Waterloo, 2009. Available: https://uwspace.uwaterloo.ca/bitstream/handle/10012/4297/Alimardani_Masoud.pdf?sequence=1.

[8] X. Gong, Y. Zhang, and M. Liu, “Powder transport model for laser cladding by lateral powder feeding: I. Powder flow field with cylindrical distribution,” Int. J. Adv. Manuf. Technol., vol. 67, no. 9–12, pp. 2501–2509, 2012.

[9] S. Carty, I. Owen, and W. Steen, “Catchment efficiency for novel nozzle designs used in laser cladding and alloying,” in Laser Processing: Surface Treatment and Film Deposition, 1996, pp. 395–410.

[10] J. Brockmann and J. Torczynski, “Aerodynamic beam generator for large particles,” 2002.

[11] D. Keicher and W. Miller, “Multiple beams and nozzles to increase deposition rate,” US Pat. 6,268,584, 2001.

[12] F. Settimo, P. Bevilacqua, and P. Rem, “Eddy current separation of fine non-ferrous particles from bulk streams,” Physical Separation in Science and Engineering, vol. 13, no. 1, pp. 15-23, 2004.

[13] H. Naidu, “Electrodynamic separation of metallic granules from mixed waste stream,” The University of Utah, 2010.

[14] E. Schloemann, “Eddy-current techniques for segregating nonferrous metals from waste,” Conserv. Recycl., vol. 5, no. 2–3, pp. 149–162, 1982.

[15] D. E. Separator, M. Lungu, and P. Rem, “Separation of small nonferrous particles using an inclined drum eddy-current separator with permanent magnets,” IEEE Trans. Magn., vol. 38, no. 3, pp. 1534–1538, 2002.

[16] V. Dyadin, V. Kozhevnikov, A. Kozyrev and N. Sochugov, “Pulsed electrodynamic separation of small conducting particles,” Russ. Phys. J., 2007.

[17] Lindsey Kratochwill, “A New Boeing Patent Describes Levitating 3D Printing,” 2016. [Online]. Available: http://www.popsci.com/new-boeing-patent-describes-levitating-3d-printing.

[18] L. Gao, Z. Shi, D. Li, G. Zhang, Y. Yang, and A. McLean, “Applications of Electromagnetic Levitation and Development of Mathematical Models: A Review of the Last 15 Years (2000 to 2015),” Mater. Trans. B, 2016.

[19] M. Reiser, Theory and design of charged particle beams. 2008.

[20] D. Heddle, Electrostatic lens systems. 2000.

[21] S. Afshar, M. B. Khamesee and A. Khajepour, “MIMO regulation control design for magnetic steering of a ferromagnetic particle inside a fluidic environment,” International Journal of Control, vol. 88, no. 10, pp. 1942-1962, 2015.

[22] R. R. Unocic and J. N. DuPont, “Process efficiency measurements in the laser engineered net shaping process,” Metall. Mater. Trans. B, vol. 35, no. 1, pp. 143–152, Feb. 2004.

[23] P. M. Sammons, D. A. Bristow, R. G. Landers, “DC-gain layer-to-layer stability criterion in laser metal deposition processes,” in Proceedings of the SFF Symposium, 2015, Texas [Online]. Available: https://sffsymposium.engr.utexas.edu/sites/default/files/2015/2015-108-Sammons.pdf. [Accessed: February, 2018].

[24] “Sources of magnetic fields,” *web.mit.edu*, n. d. [Online], pages 7 - 9, 35 – 39. Available: http://web.mit.edu/viz/EM/visualizations/coursenotes/modules/guide09.pdf and https://ocw.mit.edu/, (MIT open courseware) [Accessed: February, 2018].

[25] E. Dennison, “Off-axis field of a current loop,” *nbviewer.jupyter.org*, 2015. [Online]. Available: http://nbviewer.jupyter.org/github/tiggerntatie/emagnet-py/blob/master/offaxis/off_axis_loop.ipynb. [Accessed: February, 2018].

[26] J. Hawley, “The magnetic field in and around a finite cylindrical air-core solenoid,” *jimhawley.ca*, September, 2011. [Online]. Available: http://www.jimhawley.ca/downloads/Magnetic_Field_Around_Finite_Solenoid.pdf. [Accessed: February, 2018].

[27] J. Simpson, J. Lane, C. Immer, R. Youngquist, “Simple analytic expressions for the magnetic field of a circular current loop,” *ntrs.nasa.gov*, January 1, 2001. [NASA technical reports server, Online]. Available: https://ntrs.nasa.gov/search.jsp?R=20010038494. [Accessed: February, 2018].

[28] E. P. Ferlani, Permanent Magnet and Electromechanical Devices. New York: Academic Press, 2001, pp. 131, 135-136.

[29] J. J. Abbott, O Ergeneman, M. P. Kummer, A. M. Hirt, B. J. Nelson. “Modeling magnetic torque and force for controlled manipulation of soft-magnetic bodies,” *IEEE Transactions on Robotics*, vol. 23, no. 6, pp. 1247-1252, December, 2007.

[30] T. Al-Dulaimi, M. B. Khamesee. “A stationary apparatus of magnetic abrasive finishing using a rotating magnetic field,” *Microsyst Technol*, vol. 23, pp. 5185-5191, Springer-Verlag Berlin Heidelberg, December 2, 2016.

[31] T. Nakamura, M. B. Khamesee. “A prototype mechanism for three-dimensional levitated movement of a small magnet,” IEEE/ASME Transactions on Mechatronics, vol. 2, no. 1, pp. 41-50, March 1997.

[32] M. B. Khamesee, N. Kato, Y. Nomura. “Design and control of a microrobotic system using magnetic levitation,” *IEEE/ASME Transactions on Mechatronics*, vol. 7, no. 1, pp. 1-14, March 2002.

[33] K. R. Demarest, *Engineering Electromagnetics*. New Jersey: Prentice Hall, Inc., 1998, pp. 249-250.

[34] V. Fallah, *Solidification in laser powder deposition of Ti-Nb alloys*. PhD [Thesis, Online]. Waterloo: University of Waterloo, 2011. Available: https://uwaterloo.ca/mechatronic-vehicle-systems-lab/sites/ca.mechatronic-vehicle-systems-lab/files/uploads/files/v_fallah_t.pdf.

[35] Y. Sakurai. “Magnetic levitation of an iron ball,” Journal of Applied Physics, vol. 104, pp. 044503: 1-6, August 2008.

[36] *Aerosols*. California Institute of Technology, pp. 290-357. [Online]. Available: https://authors.library.caltech.edu/25069/7/AirPollution88-Ch5.pdf.

[37] Y. Huang, M. B. Khamesee, E. Toyserkani. “A comprehensive analytical model for laser powder-fed additive manufacturing,” *Additive Manufacturing*, vol. 12, pp. 90-99, July 2016.

[38] “Is the Earth an Electromagnetic Coil, Step up or down Transformer?” *xearththeory.com*, June 2012. [Online]. Available: http://www.xearththeory.com/earth-electromagnetic-coil-transformer/. [Accessed: February, 2018].

Appendix A

Matlab Code for Summations

```
% '// Generalized subroutine to calculate the components of the magnetic
% '// field at stepped 1mm planar points (zplane) above a cylindrical
% '// air-core solenoid. Adapted from:
% '// http://www.jimhawley.ca/downloads/Magnetic_Field_Around_Finite_Solenoid.pdf
% '//
% '// Nturns = number of turns of wire in each layer
% '// Nlayers = number of layers of wire in the winding
% '// I = current flow, in amperes
% '// Rcore = inner radius of the winding, in meters
% '// Hcoil = height of winding, in meters
% '// *** Note that Dwire, the diameter of the wire, is calculated from Hcoil / Nturns ***
% '// U = permeability of the medium, in T/Am
% '// Ntheta = number of arcs into which each turn is divided (1000 is good)
% '// Pz = axial displacement from center of coil to point P, in meters
% '// Pr = radial displacement from centerline of coil to point P, in meters
% '// Pphi = angular displacement of point P from the x-axis, in radians
% '// Bx, By, Bz = components of the magnetic field at vector P, in Tesla
clear
clc
I = 0.0624;% [A]
Bx=0;By=0;Bz=0;
Nturns=287;
Nlayers=16;
Ntheta=1000;
Rcore=0.01;% [m]
Hcoil=0.000349*Nturns;% [m] 0.577 mm film-coated
Dwire=Hcoil/Nturns;
zplane=0.01:0.01:0.03;% [m]
U=4*pi*1e-7;% mu-not
Pr=-0.200;Pz=Hcoil/2+zplane;Pphi=0;
Bxx=zeros(Rcore/0.001+191+200,1);Byy=zeros(Rcore/0.001+191+200,1);Bzz=zeros(Rcore/0.001+191+200,1);
count=0;
v=datestr(now);
for i = 1:3
for R = 1:2*(Rcore+0.190)/0.001+1
   for M = 1:Nlayers
      rMthlayer=Rcore+(Dwire*(M-0.5));
      for N = 1:Nturns
         zNthturn=Dwire*(N-0.5-(Nturns/2));
         Denominator1=(Pr*Pr)+((Pz(i)-zNthturn)*(Pz(i)-zNthturn))+(rMthlayer*rMthlayer);
         %Loop which steps around a single turn
         for Itheta = 1:Ntheta
```

```
        Theta=2*pi*(Itheta-0.5)/Ntheta;
        CosTheta=cos(Theta);
        SinTheta=sin(Theta);
        CosThetaPhi=cos(Theta-Pphi);
        Denominator2=Denominator1-(2*Pr*rMthlayer*CosThetaPhi);
        Denominator2=Denominator2*sqrt(Denominator2);
        Denominator2=rMthlayer*(2*pi/Ntheta)/Denominator2;
        dBx=(Pz(i)-zNthturn)*CosTheta*Denominator2;
        dBy=(Pz(i)-zNthturn)*SinTheta*Denominator2;
        dBz=(rMthlayer-(Pr*CosThetaPhi))*Denominator2;
        Bx=Bx+dBx;
        By=By+dBy;
        Bz=Bz+dBz;
      end% Itheta
    end% N turns
  end% M layers
  Bx=I*U*Bx/(4*pi);
  By=I*U*By/(4*pi);
  Bz=I*U*Bz/(4*pi);
  Bxx(R,i)=Bx;
  Byy(R,i)=By;
  Bzz(R,i)=Bz;
  Bx=0;By=0;Bz=0;
  Pr=Pr+0.001;
end% R
Pr=-0.200;
end

v
datestr(now)

figure
X=-0.200:0.001:Rcore+0.190;
plot(X'*1000,Bxx(:,1)*10000,'k')
hold on
plot(X'*1000,Bxx(:,2)*10000,'k--')
plot(X'*1000,Bxx(:,3)*10000,'k:')
title({'B_x (Gauss) vs. radial displacement (mm)';'(various axial displacements)'})
xlabel('Distance from centerline (mm)')
ylabel('B_x field strength (Gauss)')
ytickformat('%.1f')
xlim([-200 200])
xticks([-200 -160 -120 -80 -40 0 40 80 120 160 200])
ylim([-4.0 4.0])
legend('10mm above top turn','20','30','Location','northeast')
```

```
grid on
figure
plot(X'*1000,Bzz(:,1)*10000,'k')
hold on
plot(X'*1000,Bzz(:,2)*10000,'k--')
plot(X'*1000,Bzz(:,3)*10000,'k:')
title({'B_z (Gauss) vs. radial displacement (mm)';'(various axial displacements)'})
xlabel('Distance from centerline (mm)');
ylabel('B_z field strength(Gauss)');
ytickformat('%.1f')
xlim([-200 200])
xticks([-200 -160 -120 -80 -40 0 40 80 120 160 200])
ylim([-1.0 8.0])
legend('10mm above top turn','20','30','Location','northeast')
grid on
```

Appendix B

Matlab Code for Elliptic

```
% '// Generalized subroutine to calculate the components of the magnetic field at
% '// stepped 1mm planar points (meshgrid) above a cylindrical air/iron-core solenoid.
% '// Equations from:
% '// http://nbviewer.jupyter.org/github/tiggerntatie/emagnet-
py/blob/master/offaxis/off_axis_loop.ipynb
% '// and [27]
% '// from https://ntrs.nasa.gov/archive/nasa/casi.ntrs.nasa.gov/20010038494.pdf
% '// Nturns = number of turns of wire in each layer
% '// N_radial_layers = number of layers of wire in the winding
% '// I = current flow, in amperes
% '// a_0 = inner radius of the winding, in meters
% '// Hcoil = height of winding, in meters
% '// *** Note that Dwire, the diameter of the wire, is calculated from Hcoil / Nturns ***
% '// mu_0 = permeability of the medium, in T/Am
% '// Bx, Bz = components of the magnetic field at vector P, in Tesla
clear
clc
mu_0 = 4*pi*1e-7;% [H/m]
I=0.0624;% [A]
a_0 = 0.010+0.000349/2;% innermost current loop radius [m]
N_radial_layers = 16;% number of radial layers
N_turns = 287;% number of longitudinal loops
Hcoil=0.000349*N_turns;% coil height [m]
d = Hcoil/N_turns;% #28 gauge enameled copper wire diameter including insulation [m]
Bx_total = 0; Bz_total = 0;% initialize incrementals Bx_total, Br_total

count=0;
v=datestr(now);

[r,z]=meshgrid(linspace(-.200,.200,401),linspace(.010,.030,3));
y=0;
RHO=(r.^2+y.^2).^0.5;
GAMMA=r.^2-y.^2;
C=mu_0*I/pi;

  for x = 1:N_turns
    z_new=z+(x-1)*d;
    R=(r.^2+y.^2+z_new.^2).^0.5;
    for a = 1:N_radial_layers
      A=a_0+(a-1)*d;
      ALPHA=(A^2+R.^2-2*A*RHO).^0.5;
```

```
        BETA=(A^2+R.^2+2*A*RHO).^0.5;
        k=(1-ALPHA.^2./BETA.^2).^0.5;
        [K,E] = ellipke(k.^2);
        Bx=((C*r.*z_new)./(2*ALPHA.^2.*BETA.*RHO.^2)).*((A^2+R.^2).*E-ALPHA.^2.*K);
        Bz=(C./(2*ALPHA.^2.*BETA)).*((A^2-R.^2).*E+ALPHA.^2.*K);
        Bx_total = Bx_total+Bx;
        Bz_total = Bz_total+Bz;
    end
  end
  Bxx = Bx_total;%.*ICx; Bzz = Bz_total.*ICz;
  Bzz = Bz_total;
Bxx(isnan(Bxx))=0;
v
datestr(now)

figure
plot(-200:1:200,Bxx(1,:)*10000,'k')
hold on
plot(-200:1:200,Bxx(2,:)*10000,'k--')
plot(-200:1:200,Bxx(3,:)*10000,'k:')
xlabel('Distance from centerline (mm)')
ylabel('B_x field strength (Gauss)')
ytickformat('%.1f')
xlim([-200 200])
xticks([-200 -160 -120 -80 -40 0 40 80 120 160 200])
ylim([-4.0 4.0])
title({'B_x (Gauss) vs. radial displacement (mm)';'(various axial displacements)'})
legend('10 mm above top turn','20','30','Location','northeast')
grid on

figure
plot(-200:1:200,Bzz(1,:)*10000,'k')
hold on
plot(-200:1:200,Bzz(2,:)*10000,'k--')
plot(-200:1:200,Bzz(3,:)*10000,'k:')
xlabel('Distance from centerline (mm)')
ylabel('B_z field strength (Gauss)')
ytickformat('%.1f')
xlim([-200 200])
xticks([-200 -160 -120 -80 -40 0 40 80 120 160 200])
ylim([-1.0 8.0])
title({'B_z (Gauss) vs. radial displacement (mm)';'(various axial displacements)'})
legend('10 mm above top turn','20','30','Location','northeast')
grid on
```

Appendix C

Matlab Code for Force

```
% '// Generalized subroutine to calculate the components of the magnetic field at
% '// stepped 1mm planar points (meshgrid) above a cylindrical air/iron-core solenoid.
% '// Equations from:
% '// http://nbviewer.jupyter.org/github/tiggerntatie/emagnet-
py/blob/master/offaxis/off_axis_loop.ipynb
% '// and
% '// [27]
% '// from https://ntrs.nasa.gov/archive/nasa/casi.ntrs.nasa.gov/20010038494.pdf
% '//
% '// Also the gradient equation partials and magnetization are used to
% '// evaluate the electromagnetic force components developed on a 1mm
% '// diameter particle for comparison to COMSOL modelling
% '//
% '// Nturns = number of turns of wire in each layer
% '// N_radial_layers = number of layers of wire in the winding
% '// I = current flow, in amperes
% '// a_0 = inner radius of the winding, in meters
% '// Hcoil = height of winding, in meters
% '// *** Note that Dwire, the diameter of the wire, is calculated from Hcoil / Nturns ***
% '// mu_0 = permeability of the medium, in T/Am
% '// Bx, Bz = components of the magnetic field at vector P, in Tesla
clear
clc
mu_0 = 4*pi*1e-7;% [H/m]
IC = 1;%iron core factor for B magnification
ICx = 1;
ICz = 1;
I=0.0624;% [A]
a_0 = 0.010+0.000349/2;% innermost current loop radius [m]
N_radial_layers = 16;% number of radial layers
N_turns = 287;% number of longitudinal loops
Hcoil=0.000349*N_turns;% coil height [m]
d = Hcoil/N_turns;% #28 gauge enameled copper wire diameter including insulation [m]
Bx_total = 0; Bz_total = 0;% initialize incrementals Bx_total, Br_total
dBxdx_total=0; dBxdy_total=0; dBxdz_total=0;
dBydx_total=0; dBydy_total=0; dBydz_total=0;
dBzdx_total=0; dBzdy_total=0; dBzdz_total=0;

count=0;
v=datestr(now);

```

```
[r,z]=meshgrid(linspace(-.200,.200,401),linspace(.010,.030,3));
y=0;
RHO=(r.^2+y.^2).^0.5;
GAMMA=r.^2-y.^2;
C=mu_0*I/pi;

    for x = 1:N_turns
        z_new=z+(x-1)*d;
        R=(r.^2+y.^2+z_new.^2).^0.5;
        for a = 1:N_radial_layers
            A=a_0+(a-1)*d;
            ALPHA=(A^2+R.^2-2*A*RHO).^0.5;
            BETA=(A^2+R.^2+2*A*RHO).^0.5;
            k=(1-ALPHA.^2./BETA.^2).^0.5;
            [K,E] = ellipke(k.^2);
            Bx=((C*r.*z_new)./(2*ALPHA.^2.*BETA.*RHO.^2)).*((A^2+R.^2).*E-ALPHA.^2.*K);
            Bz=(C./(2*ALPHA.^2.*BETA)).*((A^2-R.^2).*E+ALPHA.^2.*K);
            % Gradients
            dBxdx=((C*z_new)./(2*ALPHA.^4.*BETA.^3.*RHO.^4)).*((A^4*(-
GAMMA.*(3*z_new.^2+A^2)+RHO.^2.*(8*r.^2-y^2))-A^2*(RHO.^4.*(5*r.^2+y^2)-
2*RHO.^2.*z_new.^2.*(2*r.^2+y^2)+3*z_new.^4.*GAMMA)-
R.^4.*(2*r.^4+GAMMA.*(y^2+z_new.^2))).*E+(A^2*(GAMMA.*(A^2+2*z_new.^2)-RHO.^2.*(3*r.^2-
2*y^2))+R.^2.*(2*r.^4+GAMMA.*(y^2+z_new.^2))).*ALPHA.^2.*K);
            dBxdy=((C*r.*z_new*y)./(2*ALPHA.^4.*BETA.^3.*RHO.^4)).*((3*A^4*(3*RHO.^2-
2*z_new.^2)-R.^4.*(2*R.^2+RHO.^2)-2*A^6-2*A^2*(2*RHO.^4-
RHO.^2.*z_new.^2+3*z_new.^4)).*E+(R.^2.*(2*R.^2+RHO.^2)-A^2*(5*RHO.^2-
4*z_new.^2)+2*A^4).*ALPHA.^2.*K);
            dBxdz=((C*r)./(2*ALPHA.^4.*BETA.^3.*RHO.^2)).*(((RHO.^2-
A^2).^2.*(RHO.^2+A^2)+2*z_new.^2.*(A^4-6*A^2*RHO.^2+RHO.^4)+z_new.^4.*(A^2+RHO.^2)).*E-
((RHO.^2-A^2).^2+z_new.^2.*(RHO.^2+A^2)).*ALPHA.^2.*K);
            dBydx=dBxdy;

dBydy=((C*z_new)./(2*ALPHA.^4.*BETA.^3.*RHO.^4)).*((A^4*(GAMMA.*(3*z_new.^2+A^2)+RHO.^2.
*(8*y^2-r.^2))-A^2*(RHO.^4.*(5*y^2+r.^2)-2*RHO.^2.*z_new.^2.*(2*y^2+r.^2)-3*z_new.^4.*GAMMA)-
R.^4.*(2*y^4-GAMMA.*(r.^2+z_new.^2))).*E+(A^2*(-GAMMA.*(A^2+2*z_new.^2)-RHO.^2.*(3*y^2-
2*r.^2))+R.^2.*(2*y^4-GAMMA.*(r.^2+z_new.^2))).*ALPHA.^2.*K);
            dBydz=(y./x).*dBxdz;
            dBzdx=dBxdz;
            dBzdy=dBydz;
            dBzdz=((C*z_new)./(2*ALPHA.^4.*BETA.^3)).*((6*A^2*(RHO.^2-z_new.^2)-
7*A^4+R.^4).*E+ALPHA.^2.*(A^2-R.^2).*K);
            Bx_total = Bx_total+Bx;
            Bz_total = Bz_total+Bz;
            dBxdx_total=dBxdx_total+dBxdx;
            dBxdy_total=dBxdy_total+dBxdy;
```

```
        dBxdz_total=dBxdz_total+dBxdz;
        dBydx_total=dBydx_total+dBydx;
        dBydy_total=dBydy_total+dBydy;
        dBydz_total=dBydz_total+dBydz;
        dBzdx_total=dBzdx_total+dBzdx;
        dBzdy_total=dBzdy_total+dBzdy;
        dBzdz_total=dBzdz_total+dBzdz;
    end
  end
  Bxx = Bx_total;%.*ICx; Bzz = Bz_total.*ICz;
  Bzz = Bz_total;

Fx=dBzdx_total.*ICx;
Fz=dBzdz_total.*ICz;
Gx=dBxdx_total.*ICx;
Gz=dBxdz_total.*ICz;

Bxx(isnan(Bxx))=0;

v
datestr(now)

Mx=ICx*(1/mu_0-1/(4000*mu_0)).*Bxx;% Magnetization x
Mz=ICz*(1/mu_0-1/(4000*mu_0)).*Bzz;% Magnetization z

Force_contr_x=(Mx.*Gx+Mz.*Gz);
Force_contr_x(isnan(Force_contr_x))=0;
Force_contr_z=(Mx.*Fx+Mz.*Fz);
Diameter = [0.000125 0.0005 0.0010 0.0015 0.002];
Volume = 4/3*pi.*(Diameter./2).^3;
Force_x=Force_contr_x*Volume(1,1);
Force_z=Force_contr_z*Volume(1,1);
for i = 2:5
Force_x=cat(3,Force_x,Force_contr_x*Volume(1,i));
Force_z=cat(3,Force_z,Force_contr_z*Volume(1,i));
end

X=Force_x(:,:,3);
Z=Force_z(:,:,3);

figure
plot(r(1,:)*1000,Force_x(1,:,3),'k')
hold on
plot(r(1,:)*1000,Force_x(2,:,3),'k--')
plot(r(1,:)*1000,Force_x(3,:,3),'k:')
xlabel('Distance from centerline (mm)')
ylabel('F_x (N)')
```

```
ytickformat('%.1f')
xlim([-200 200])
xticks([-200 -160 -120 -80 -40 0 40 80 120 160 200])
ylim([-6.0e-9 6.0e-9])
title({'Force x-comp (N) vs. radial displacement (mm)';'(various axial displacements)'})
legend('10 mm above top turn','20','30','Location','northeast')
grid on

figure
plot(r(1,:)*1000,Force_z(1,:,3),'k')
hold on
plot(r(1,:)*1000,Force_z(2,:,3),'k--')
plot(r(1,:)*1000,Force_z(3,:,3),'k:')
xlabel('Distance from centerline (mm)')
ylabel('F_z (N)')
ytickformat('%.1f')
xlim([-200 200])
xticks([-200 -160 -120 -80 -40 0 40 80 120 160 200])
ylim([-20.0e-9 0.0e-9])
ax = gca;
ax.YAxis.Exponent = -9;
yticks([-20e-9 -18e-9 -16e-9 -14e-9 -12e-9 -10e-9 -8e-9 -6e-9 -4e-9 -2e-9 0e-9])
title({'Force z-comp (N) vs. radial displacement (mm)';'(various axial displacements)'})
legend('10 mm above top turn','20','30','Location','northeast')
grid on
```

NOTE: lines 94 and 95 in the above assume B is that produced by the magnetic construct and not the iron particle (B_{sat}). In [28] the equations involve a magnet as the source of B as opposed to B_{ext} used in the remainder of (4.17). This can be attributed to the variation between analytical and simulation (FEA) results, and the FEA results were taken to govern.

Regarding the above code, if ICx and ICz in lines 25 and 26 are held at 1 the force plots are then comparable to those of the COMSOL simulation within about 20 percent. The discrepancy between the B field results of Figure 4.10 and Figure 4.11 is in a similar range. This is for air core.

For iron core, regarding the above code, if ICx and ICz in lines 25 and 26 are given as 10 instead of 1, the force plots are then comparable to those of the COMSOL simulation, once lines 122, 137, and 140 have their data multiplied by 10*10, or 100, in the Matlab code, above. The B field here is also approximately 10 times that of the air core.

Appendix D

Matlab Code and Function for Trajectory

```
clear;clc;datestr(now)
timestep = 0.011;timerange = 0:timestep/110:timestep;% time interval in seconds for given particle and magnet configuration at speed of 2m/s
%**************************************************************************
angle = 0;% angle of powder stream in radians/degrees from vertical
% particle initial conditions (x and z)
% initialvalues = [x vx z vz]
for q = 1:10
initialvalues = [0.001*q 2*sin(angle) 0.02 -2*cos(angle)];% initial x and z values in m and m/s
%**************************************************************************
[t,x]=ode45(@f_old,timerange,initialvalues);
new_x(:,:,q) = x;% new position/velocity matrix (to be updated each x-position change)
end

figure
plot(new_x(:,1,1)*1000,new_x(:,3,1)*1000,'c')
ylabel('z-position (mm) from PM top')
xlabel('x-position (mm) from PM axis')
axis([0 10 0 20])
grid on
hold on
plot(new_x(:,1,2)*1000,new_x(:,3,2)*1000,'r')
plot(new_x(:,1,3)*1000,new_x(:,3,3)*1000,'b')
plot(new_x(:,1,4)*1000,new_x(:,3,4)*1000,'m')
plot(new_x(:,1,5)*1000,new_x(:,3,5)*1000,'g')
plot(new_x(:,1,6)*1000,new_x(:,3,6)*1000,'c')
plot(new_x(:,1,7)*1000,new_x(:,3,7)*1000,'r')
plot(new_x(:,1,8)*1000,new_x(:,3,8)*1000,'b')
plot(new_x(:,1,9)*1000,new_x(:,3,9)*1000,'m')
plot(new_x(:,1,10)*1000,new_x(:,3,10)*1000,'g')
legend('x_0 = 1','x_0 = 2','x_0 = 3','x_0 = 4','x_0= 5','x_0 = 6','x_0 = 7','x_0 = 8','x_0 = 9','x_0 = 10','Location','northeast')
title('Particle position relative to PM axis, top of coil, D_p = 0.125mm')
```

```
1  function rk = f_old(t,x)
2  %*********************************************************************
3  % change Dp to 0.001 for 1mm diameter particle, 0.0015 for 1.5mm,...:
4  % Dp = 0.001;%particle diameter in m
5  Dp = 0.000125;%particle diameter in m
6  %*********************************************************************
7  Cd = 0.44;% drag coefficient
8  rho_arg = 1.6339;% density of argon at 25 C and 14.696 psia in kg/m^3
9  rho_iron = 7800;% density of iron (assumed) [kg/m^3]
10 M = 4/3*pi*(Dp/2)^3*rho_iron;% mass of iron particle in kg
11 D = pi/8*Cd*rho_arg*Dp^2;% drag contribution of velocity
12 g = 9.80;% gravity acceleration [m/s^2]
13 load('FxFz1mm_PM_1inch_square_dimpled_10_4')
14
15 Fx = Fx*1e-6;
16 Fz = Fz*1e-6;
17 X = 1:27; Z = 1:20;%
18 ff=interp2(X,Z,Fx,x(1)*1000+14,x(3)*1000);
19 gg=interp2(X,Z,Fz,x(1)*1000+14,x(3)*1000);
20 dx(1) = x(2);
21 dx(2) = -D/M*sign(x(2)).*x(2).^2+1/M*ff;
22 dx(3) = x(4);
23 dx(4) = D/M*x(4).^2+1/M*gg-g
24 rk = [dx(1);dx(2);dx(3);dx(4)]
```

NOTE: In line 13 of the above a special file structure of the loaded file is required and this impacts lines 17, 18 and 19.

Appendix E

Magnetic Field Gradients

The following equations and figure presented from [27] describe the magnetic field gradient with respect to the circular current loop of Figure 4.12. Superposition was used in their application to approximate the force on an iron particle from an air core solenoid in Matlab. The same simple substitutions from subsection 4.3.2 are used. They also make use of complete elliptic integrals of the first and second kind.

Spatial Derivatives of the Magnetic Field Components:

$$\begin{aligned}\frac{\partial B_x}{\partial x} = \frac{Cz}{2\alpha^4\beta^3\rho^4}\{&\left[a^4\left(-\gamma(3z^2+a^2)+\rho^2(8x^2-y^2)\right)\right.\\&-a^2(\rho^4(5x^2+y^2)-2\rho^2z^2(2x^2+y^2)+3z^4\gamma)\\&\left.-r^4\left(2x^4+\gamma(y^2+z^2)\right)\right]E(k^2)\\&+\left[a^2\left(\gamma(a^2+2z^2)-\rho^2(3x^2-2y^2)\right)\right.\\&\left.+r^2\left(2x^4+\gamma(y^2+z^2)\right)\right]\alpha^2K(k^2)\}\end{aligned} \tag{7.1}$$

$$\begin{aligned}\frac{\partial B_x}{\partial y} = \frac{Cxyz}{2\alpha^4\beta^3\rho^4}\{&[3a^4(3\rho^2-2z^2)-r^4(2r^2+\rho^2)-2a^6\\&-2a^2(2\rho^4-\rho^2z^2+3z^4)]E(k^2)\\&+[r^2(2r^2+\rho^2)-a^2(5\rho^2-4z^2)+2a^4]\alpha^2K(k^2)\}\end{aligned} \tag{7.2}$$

$$\begin{aligned}\frac{\partial B_x}{\partial z} = \frac{Cx}{2\alpha^4\beta^3\rho^2}\{&[(\rho^2-a^2)^2(\rho^2+a^2)+2z^2(a^4-6a^2\rho^2+\rho^4)\\&+z^4(a^2+\rho^2)]E(k^2)-[(\rho^2-a^2)^2+z^2(\rho^2+a^2)]K(k^2)\}\end{aligned} \tag{7.3}$$

$$\frac{\partial B_y}{\partial x} = \frac{\partial B_x}{\partial y} \tag{7.4}$$

$$\begin{aligned}\frac{\partial B_y}{\partial y} = \frac{Cz}{2\alpha^4\beta^3\rho^4}\{&\left[a^4\left(\gamma(3z^2+a^2)+\rho^2(8y^2-x^2)\right)\right.\\&-a^2(\rho^4(5y^2+x^2)-2\rho^2z^2(2y^2+x^2)-3z^4\gamma)\\&\left.-r^4\left(2y^4-\gamma(x^2+z^2)\right)\right]E(k^2)\\&+\left[a^2\left(-\gamma(a^2+2z^2)-\rho^2(3y^2-2x^2)\right)\right.\\&\left.+r^2\left(2y^4-\gamma(x^2+z^2)\right)\right]\alpha^2K(k^2)\}\end{aligned} \tag{7.5}$$

$$\frac{\partial B_y}{\partial z} = \frac{y}{x}\frac{\partial B_x}{\partial z} \tag{7.6}$$

$$\frac{\partial B_z}{\partial x} = \frac{\partial B_x}{\partial z} \tag{7.7}$$

$$\frac{\partial B_z}{\partial y} = \frac{\partial B_y}{\partial z} \tag{7.8}$$

$$\frac{\partial B_z}{\partial z} = \frac{Cz}{2\alpha^4\beta^3}\{[6a^2(\rho^2 - z^2) - 7a^4 + r^4]E(k^2) + \alpha^2[a^2 - r^2]K(k^2)\} \tag{7.9}$$

Variables in the above are as explained in subsection 4.3.2.

To further simplify, the above nine derivatives can be reduced to seven when y is set equal to zero. Also the magnetic field y component will be zero reducing this set to four (M_y=0) when y is set equal to zero for planar x-z analysis.

Appendix F
Proposed Experimental Studies

Although some experimental efforts were carried out, their results were inconclusive due to lack of processing capabilities and disproved methodologies. In their place, the following is provided as a description of proposed study.

A proof of concept proposal is first presented, then Main 1 and Main 2 (no laser) describe proposed methods for future experiments.

Proof of Concept

A proof of concept method was proposed involving the introduction of a 10mm diameter, 10mm height N42 permanent magnet to an AM ferromagnetic powder stream path. Still photographs of the powder stream without and with the magnet present would be compared to verify a change in shape (intensity) of the stream in the vicinity of the area above the magnet. This would act as a strong positive to authenticate the experimental viability and justify more intensive efforts. If no change was immediately discernable with the 10mm N42 then stronger magnets, or magnets of more bulk, could be simulated and then experimentally attempted, to provide verification.

Main 1 is presented, next.

Main 1

Here, an apparatus is proposed to simulate powder stream deposition on the substrate. It is presented in Figure F. 1 and its use is described as follows.

- Item 3 of Figure F. 1 secures the right assembly of Figure F. 1 to a CNC apparatus
- A permanent magnet seats on the bolt on the lower left of the right assembly, vertically beneath the stationary powder stream (the right assembly is stationary)
- Item 7 clamps in a 3-jaw chuck of the CNC which provides the translational motion of Item 11, the substrate
- Alignment to preserve linear powder deposition is set before the deposition proceeds

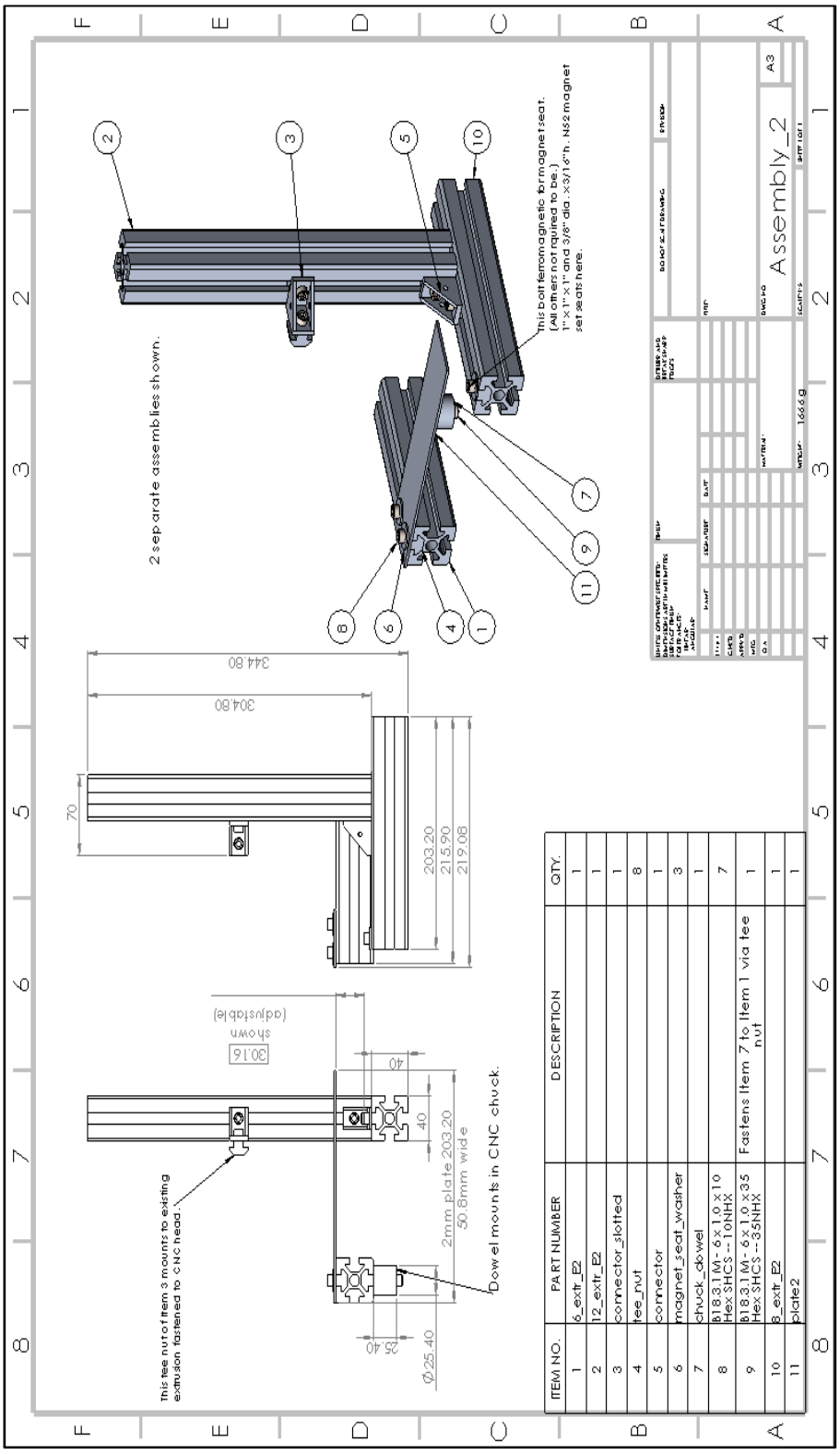

Figure F. 1: Proposed Main experimental apparatus

Still photographs of the powder stream without, and with a PM present on the magnet seat are proposed to verify the shape change (intensity) of the stream in the vicinity of the area above the magnet.

The one inch dimpled cube of Figure 5.7 with laser operation, and without, is described, next.

One inch dimpled cube of Figure 5.7 with laser

Use of the laser is proposed here to carry out an actual additive run. With the one inch cube N52 PM beneath the substrate, an approximate 700W laser energy beam would create the clad from content of the powder stream. Multiple clad paths for each substrate blank would have the substrate alternately clad and weighed and compared to a second substrate blank that was clad without the presence of the magnet beneath.

Weight results obtained here could then be used to comparatively determine the catchment efficiency as a relative percentage improvement (substrate without magnet present and with magnet present). Photographic evidence of the stream shape change would not be practical because of the use of the laser, here, as well as the additional complication of an angled powder stream.

One inch dimpled cube of Figure 5.7, no laser

Here, a completely vertical powder stream is proposed with completely unobscured visibility of the powder stream. This would allow still photographs to verify shape change of the stream in the vicinity of the area above the magnet. Foreseen difficulties with magnetic drag of the deposited particles represents a complication which would need to be overcome.

Main 2 is presented, next.

Main 2 (no laser)

Main 2 (no laser) involves a proposal of the bulleted process outlined in Main 1 and the description of the above subsection, “One inch dimpled cube of Figure 5.7, no laser,” using the PM configurations suggested in the closing of section 6.3. These configurations are again listed, below.

2. a 10mm diameter by 10mm height PM with a 4mm diameter by 1.5mm height PM atop,
3. a 25.4mm diameter PM, of 19.05mm height, with a 2mm diameter by 4mm height PM atop, and
4. a 25.4mm diameter PM, of 19.05mm height, with a 4mm diameter by 1.5mm height PM atop.

Glossary

Additive manufacturing (AM) is the process by which an object is built with the use of stratified, layer-by-layer construction, controlled via computer software (iii, 1, 2, 3, 5, 6, 7, 9, 11, 12, 15, 16, 23, 48, 49, 57, and 58)

Catchment efficiency is the ability of a process to have a significant portion of a powder or particle stream introduced to the melt zone, or active build zone in additive manufacturing (iii, 1, 2, 3, 5-10, 12, 13, 15, 57, 77).

Clad area is the area in section of the melt pool solidification which is not part of the substrate (7, 8, 9, and 12).

Drag force is the aerodynamic drag on a particle in motion in a fluid (15, 21, and 23).

Eddy current is the magnetic field developed in opposition to an existing field producing a confluence, or eddy that can introduce spin to a rotationally static particle with this opposition creating a deflecting motion (10, 11).

Electromagnetic (field) is the complimentary union of an electric and magnetic field created when an electric source is present to create the magnetic field (iii, 9).

(Electro) magnetic field gradient is described by nine directional derivatives of the magnetic field. It is the rate of change of the magnetic field (from a coil or permanent magnet) in a given direction (4, 24, 37, 39, and 73).

Electromagnetic (force) is the force generated on a ferromagnetic particle when it is in the presence of an electric field (1, 39, 43, 44, 45, 46, 47, 48, 49, 53, 54, and 60).

Complete elliptic integrals are elliptic integrals with an amplitude of $\frac{\pi}{2}$ and their full mathematical description is available in the literature. The first and second kind are used within (4, 13, 24, 29, 30, 32, 33, 34, 38, 39, 57, and 73).

Ferromagnetic particle any particle with a large positive susceptibility to an external magnetic field (iii, 1, 4, 5, 6, 9, 12, 18, 19, 37, 47, 57).

Helmholtz coil is a twin coil device which can produce a nearly uniform magnetic field between the same-axis coils which is capable of canceling external magnetic fields (12).

Magnetic field is herein considered to be the field that can be present when an electric field is present or when a magnet source such as a permanent magnet is present (several).

Magnetic dipole is deemed to be a pair of poles which in the limit of their size reduction result in a singularity (37).

Magnetic levitation is the occurrence when an object is magnetically levitated or magnetically suspended without support save the magnetic field (11, 12, 15).

Melt pool is used to describe the region of an additive manufacturing build zone which is in a liquid state (iii, 1, 2, 6, 9, 12, 15, 48, 55, 57, 58).

Neodymium is herein use to designate the class of rare earth magnets, the most powerful currently available (45).

Shielding gas is the application of the gas used to protect the additive manufacturing build zone during local laser activity to protect the melt zone from oxidation or development of other impurities (5, 16).

Solenoid is the term used to describe the coil (air or iron core), or inductor (air core) of AWG type used (iii, 1, 2, 4, 6, 13, 24, 26, 29, 31, 35, 38, 40, 43, 57, 58, 73).

Substrate is the term used to describe the base upon which the additive process proceeds, or describe the substance which is acted on (1, 2, 6, 8, 10, 16, 17, 18, 19, 55, 59, 60, 75, 77).

Subtractive manufacturing is any process where a usable part is worked or machined from a solid block of material, or blank (1, 5).